

Sussex Research

The XMM–NEWTON ? Project: I. The X-ray luminosity – temperature relation at $z>0.4$

D H Lumb, J G Bartlett, Kathy Romer, A Blanchard, D J Burke, C A Collins, R C Nichol, M Giard, P B Marty, J Nevalainen, R Sadat, S C Vauclair

Publication date

01-01-2004

Licence

This work is made available under the **Copyright not evaluated** licence and should only be used in accordance with that licence. For more information on the specific terms, consult the repository record for this item.

Citation for this work (American Psychological Association 7th edition)

Lumb, D. H., Bartlett, J. G., Romer, K., Blanchard, A., Burke, D. J., Collins, C. A., Nichol, R. C., Giard, M., Marty, P. B., Nevalainen, J., Sadat, R., & Vauclair, S. C. (2004). *The XMM–NEWTON ? Project: I. The X-ray luminosity – temperature relation at $z>0.4$* (Version 1). University of Sussex.
<https://hdl.handle.net/10779/uos.23312813.v1>

Published in

Astronomy and Astrophysics

Link to external publisher version

<https://doi.org/10.1051/0004-6361:20035687>

Copyright and reuse:

This work was downloaded from Sussex Research Open (SRO). This document is made available in line with publisher policy and may differ from the published version. Please cite the published version where possible. Copyright and all moral rights to the version of the paper presented here belong to the individual author(s) and/or other copyright owners unless otherwise stated. For more information on this work, SRO or to report an issue, you can contact the repository administrators at sro@sussex.ac.uk. Discover more of the University's research at <https://sussex.figshare.com/>

The XMM–NEWTON Ω Project: I. The X-ray Luminosity – Temperature Relation at $z > 0.4$

D. H. Lumb¹, J.G. Bartlett^{2,3}, A.K. Romer⁴, A. Blanchard⁵, D.J. Burke⁶, C.A. Collins⁷, R.C. Nichol⁴,
M. Giard⁸, P.B. Marty⁵, J. Nevalainen⁶, R. Sadat⁵, and S. C. Vauclair⁵

¹ Science Payloads and Advanced Concepts Office, European Space Agency, ESTEC, 2200AG Noordwijk, The Netherlands

² APC - Université Paris 7/PCC - Collège de France, 11, pl. Marcelin Berthelot F-75231 Paris Cedex 05, France

³ Centre de Données astronomiques de Strasbourg, 11, rue de l'Université, F-67000 Strasbourg, France

⁴ Physics Department, Carnegie Mellon University, Pittsburgh, PA 15213, USA

⁵ Laboratoire d'Astrophysique, OMP, CNRS, UPS, 14, Av Ed. Belin, 31 400, Toulouse, France

⁶ Harvard-Smithsonian Center for Astrophysics, 60 Garden Street, Cambridge, MA 02138. USA

⁷ Astrophysics Research Institute, Liverpool John Moores University, Twelve Quays House, Egerton Wharf, Birkenhead CH41 1LD, UK

⁸ Centre d'Etude Spatiale des Rayonnements, 9 avenue du Colonel Roche, BP 4346, 31028 Toulouse, France

Received date / Accepted date

Abstract. We describe XMM-Newton Guaranteed Time observations of a sample of eight high redshift ($0.45 < z < 0.62$) clusters. The goal of these observations was to measure the luminosity and the temperature of the clusters to a precision of $\sim 10\%$, leading to constraints on the possible evolution of the luminosity–temperature ($L_x - T_x$) relation, and ultimately on the values of the matter density, Ω_M , and, to a lesser extent, the cosmological constant Ω_Λ . The clusters were drawn from the SHARC and 160 Square Degree (160SD) ROSAT surveys and span a bolometric (0.0–20 keV) luminosity range of 2.0 to 14.4×10^{44} erg s^{−1} ($H_0=50, \Omega_M=1, \Omega_\Lambda=0$). Here we describe our data analysis techniques and present, for the first time with XMM-Newton, a $L_x - T_x$ relation. For each of the eight clusters in the sample, we have measured total ($r < r_{\text{virial}}$) bolometric luminosities, performed β -model fits to the radial surface profiles and made spectral fits to a single temperature isothermal model. We describe data analysis techniques that pay particular attention to background mitigation. We have also estimated temperatures and luminosities for two known clusters (Abell 2246 and RXJ1325.0-3814), and one new high redshift cluster candidate (XMMU J084701.8+345117), that were detected off-axis. Characterizing the $L_x - T_x$ relation as $L_x = L_6(\frac{T_x}{6\text{keV}})^\alpha$, we find $L_6 = 15.9^{+7.6}_{-5.2} \times 10^{44}$ erg s^{−1} and $\alpha = 2.7 \pm 0.4$ for an $\Omega_\Lambda = 0.0, \Omega_M = 1.0, H_0 = 50$ km s^{−1} Mpc^{−1} cosmology at a typical redshift $z \sim 0.55$. Comparing with the low redshift study by Markevitch, 1998, we find α to be in agreement, and assuming $L_x - T_x$ to evolve as $(1+z)^A$, we find $A = 0.68 \pm 0.26$ for the same cosmology and $A = 1.52^{+0.26}_{-0.27}$ for an $\Omega_\Lambda = 0.7, \Omega_M = 0.3$ cosmology. Our A values are very similar to those found previously by Vikhlinin et al., 2002 using a compilation of Chandra observations of $0.39 < z < 1.26$ clusters. We conclude that there is now evidence from both XMM-Newton and Chandra for an evolutionary trend in the $L_x - T_x$ relation. This evolution is significantly below the level expected from the predictions of the self-similar model for an $\Omega_\Lambda = 0.0, \Omega_M = 1.0$, cosmology, but consistent with self-similar model in an $\Omega_\Lambda = 0.7, \Omega_M = 0.3$ cosmology. Our observations lend support to the robustness and completeness of the SHARC and 160SD surveys.

Key words. X-rays:Galaxies: clusters :

1. Introduction

1.1. Motivation

As the most massive gravitationally bound objects in the universe, galaxy clusters are particularly sensitive to the evolution of the density perturbations responsible for their formation. Cluster abundance as a function of mass and redshift is dictated by the mass function (Press and Schechter, 1974; Jenkins et al., 2001), which gives the comoving space density of collapsed objects as a function of mass and redshift. In

standard models, the mass function falls off as a Gaussian at the high mass end, reflecting the Gaussian nature of the density perturbations. Galaxy cluster abundance is therefore exquisitely sensitive to the amplitude of the perturbations and its evolution. Since this evolution is controlled by the underlying cosmological background, observations of cluster abundance offer an effective way to constrain certain cosmological parameters, such as the density parameter (Oukbir & Blanchard, 1992; Blanchard and Bartlett, 1998) or the dark energy parameter and equation-of-state (Majumdar & Mohr, 2003; Wang & Steinhardt, 1998). The present day cluster abundance is degenerate in the matter

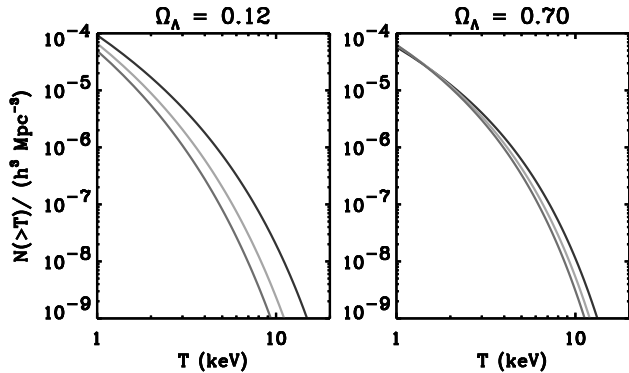


Fig. 1. The predicted X-ray temperature function at redshifts $z = 0.05$ (black), 0.33 (light grey) and 0.5 (dark grey) for a flat high density model (left; $\Omega_\Lambda = 0.12$) and a concordance model (right; $\Omega_\Lambda = 0.7$), both fitted to the local ($z \sim 0.05$) temperature function.

density and amplitude of the power spectrum; evolution of the abundance breaks this degeneracy. Constraints obtained in this manner are complementary to others that essentially rely on determinations of cosmological distances; for example, those found by observations of supernovae type Ia or by measurements of cosmic microwave background anisotropies.

Cluster mass is, however, difficult to measure directly, and in practice one seeks a direct observable that is closely related to virial mass. Lensing surveys would seem the most suited to the task, as the effects of lensing are of course directly related to mass (albeit projected along the line-of-sight). However, cluster mass estimates from weak and strong lensing remain controversial as they suffer from several systematic uncertainties (e.g. projection effects). Among X-ray observables, intracluster gas temperature is expected to be tightly correlated with virial mass, an expectation borne out by simple hydrostatic considerations as well as by numerical simulations (Evrard et al., 1996; Bryan and Norman, 1998). X-ray luminosity, on the other hand, is a much less robust mass indicator, despite being significantly easier to measure, because it depends on the density profile of the intracluster gas, the physics of which is currently difficult to model.

With a calibrated $T_x - M$ (temperature-mass) relation, the mass function can be translated into an observable cluster temperature distribution function dn/dT . The exact $T - M$ relation to use is of course a key ingredient, one that may be addressed, for example, using numerical simulations, or directly from detailed observations that determine both cluster mass and temperature (e.g. Nevalainen et al., 2000). Figure 1 compares temperature function predictions for a high matter density and a flat model, both normalized to the present-day, observed dn/dT (e.g. Henry and Arnaud, 1991; Edge et al., 1990; Blanchard et al., 2000; Ikebe et al., 2002). Evolution toward higher redshift is strikingly different in two

cosmological models *differing by their matter content alone* and illustrating the above argument.

Despite this obvious promise, it has been difficult to use $dn/dT(z)$ to explore the cosmological model because direct measurements of T_x at $z > 0$ require long integration with satellite observations. Prior to the launch of Chandra and XMM-Newton, the number of measured cluster temperatures at high redshifts was very small. This is attested to by the fact that the most distant determination of dn/dT (Henry, 2000) to date was based on a sample of only fourteen $z > 0.3$ clusters (mean ~ 0.38) from the Einstein Medium Sensitivity Survey (EMSS; Gioia et al., 1990).

An alternative, but related approach is to apply a luminosity-temperature ($L_x - T_x$) relation to a flux-limited sample, thereby obtaining either the temperature function, or a redshift distribution at given temperature (Oukbir & Blanchard, 1997; Sadat et al., 1998; Reichart et al., 1999; Borgani et al., 2000). The advantage of this approach is that it does not require detailed X-ray spectroscopy of all the clusters in a flux-limited sample to establish the $L_x - T_x$ relation and its evolution. There are now several flux limited catalogs of medium to high redshift clusters, in addition to the EMSS, to which one can apply this technique. These include those based on data from the ROSAT All Sky Survey (e.g. Ebeling, Edge, & Henry, 2001; Zhang et al., 2003), NEP (e.g. Gioia et al. (2001); Henry et al. (2001)); and from the ROSAT pointing archive (e.g. Romer et al., 2000; Burke et al., 2003; Vikhlinin et al., 1998; Mullis et al., 2003; Scharf et al. 1997; Rosati et al., 1995).

1.2. The XMM-Newton Ω -Project

The goal of the XMM-Newton Ω -project (Bartlett et al., 2001) is to increase the number of high quality X-ray cluster temperature measurements at $z > 0.3$, and thus enhance the scientific yield from the various ROSAT surveys. We describe below XMM-Newton observations of eight ROSAT clusters at $z > 0.4$ (median of $z = 0.54$) performed as part of the Guaranteed Time programme. Related observations conducted during the open time programmes of seven $0.3 < z < 0.4$ clusters are discussed elsewhere (Majerowicz, et al., 2002(b); Majerowicz, et al., 2004). Cosmological interpretation is presented in Vaclair et al, 2003. In Sections 2 & 3 we describe the observations and data analysis techniques. In Section 4 we discuss each of the eight clusters in turn. In Section 5 we present our $L_x - T_x$ relation and compare it to previous work.

This paper serves also to introduce the Project, and represents an opportunity to provide detailed descriptions of analysis techniques used in the Project and which can be used generally for XMM-Newton observations of cluster targets. Except where explicitly stated elsewhere we use a $\Omega_M = 1$, $\Omega_\Lambda = 0$, $q_0 = 0.5$ model with $H_0 = 50 \text{ km s}^{-1} \text{ Mpc}^{-1}$ that has been most frequently used in the past as the parameter set for X-ray cluster studies. When necessary for examining cosmological implications we correct our results to a concordance model.

2. Observation Programme

2.1. The Sample

Table 1 summarizes the locations, date of observations and other details of the eight clusters in this programme. Seven of the eight clusters were drawn from the SHARC Surveys, four from the Southern SHARC (Burke et al., 2003) sample and three from the Bright SHARC (Romer et al., 2000) sample. The SHARC cluster samples are based on searches for clusters serendipitously detected in ROSAT PSPC observations. They complement each other in that they cover, respectively, 17.7 degrees^2 to a flux limit of $\approx 3.9 \times 10^{-14} \text{ erg s}^{-1} \text{ cm}^{-2}$ (Collins et al., 1997) and 178.6 degrees^2 to a flux limit of $\approx 1.4 \times 10^{-13} \text{ erg s}^{-1} \text{ cm}^{-2}$ (Nichol et al., 1999). This strategy has yielded a combined cluster catalogue that straddles L^* over the redshift range $0.2 < z < 0.8$ and shows a consistent picture of a non-evolving cluster luminosity function (Collins et al., 1997; Burke et al., 1997) except, possibly, at luminosities greater than $L_x = 5 \times 10^{44} \text{ erg s}^{-1}$ (Nichol et al., 1999; Adami et al., 2000). Two aspects of the SHARC surveys, makes them particularly well suited to the XMM-Newton Ω project; they have been subjected both to detailed optical follow-up (Romer et al., 2000; Burke et al., 2003) and to extensive selection function simulations (Adami et al., 2000; Burke et al., 2003). The eighth cluster in our observation programme was taken from the 160 Square Degree ROSAT Survey (160SD hereafter, Vikhlinin et al., 1998 and Mullis et al., 2003). There is considerable overlap, both in terms of methodology and cluster members, between the 160SD and the SHARC surveys (3 of the 7 SHARC clusters are also members of the 160SD catalogue), however, this particular cluster (RXJ0847.2) was not a member of either SHARC sample because its host PSPC observation did not meet the SHARC exposure time criterion. The selection of clusters sampled in this programme was driven solely by a requirement to observe all $z \geq 0.5$ targets from the SHARC surveys. Following the visibility and observability constraints of the XMM-Newton Guaranteed Time programme we added two clusters with slightly lower redshift from the SHARC sample in addition to the one from the 160SD catalogue.

2.2. XMM-Newton

XMM-Newton (Jansen et al., 2001) comprises 3 co-aligned telescopes, each with effective area at 1.5 keV of $\sim 1500 \text{ cm}^2$, and Full Width Half Maximum (FWHM) angular resolution of $\sim 5 \text{ arc-seconds}$. This combination of the highest ever focused X-ray collection area, and the ability to resolve clusters at all redshifts, makes XMM-Newton the best suited observatory for this programme. The 3 telescopes each have a focal plane CCD imaging spectrometer camera provided by the EPIC consortium. Two also have a reflection grating array, which splits off half the light, to provide simultaneous high resolution dispersive spectra. These two telescopes are equipped with EPIC MOS cameras (Turner et al., 2001), which are conventional CMOS CCD-based imagers enhanced for X-ray sensitivity. The third employs the EPIC PN camera (Strüder et al., 2001)

which is based on a pn-junction multi-linear readout CCD. The EPIC cameras offer a field of view (FOV) of $\sim 30 \text{ arc-minute}$ diameter, and an energy resolution of typically 100 eV (FWHM) in the range $\sim 0.2\text{--}10 \text{ keV}$. The 7 CCDs in each of the MOS cameras are about $10 \text{ arc-minutes square}$ each. The central chip encompasses the whole of our $z > 0.4$ clusters. The 12 CCDs in the PN are about $4 \times 13 \text{ arc-minutes}$. Even if correctly centered on the boresight PN CCD, some portion of the target cluster emission may spill onto neighbouring CCDs, and across dead zones between CCDs. In each camera, an aluminized optical blocking filter was deployed, the thickness of which was chosen to suit the expected brightness of nearby serendipitous objects in each field. Seven of the eight clusters were observed in the Full Frame Imaging mode, as appropriate for weak extended targets, but one (RXJ1325.5) was observed when the MOS cameras were in “Window” mode, due to the presence of an unusually bright nearby point source.

The data were processed through the XMM-Newton Science Analysis Sub-System (SAS; Watson et al., 2001) version 5.3, in order to register photons from detector to sky coordinates, to correct energy data for gain and charge transfer losses, and remove instrument noise artifacts. This provided calibrated event lists as a starting point for our detailed data reduction.

3. Data Reduction

3.1. Rate Filtering

Part of the XMM-Newton orbit lies within the magnetosphere, and consequently the spacecraft can encounter clouds of protons accelerated by magnetic reconnection. When these particles scatter through the mirror system they are concentrated onto the focal plane, and an enhanced background rate can occur. These intervals were identified by forming histograms of events with energy $\geq 10 \text{ keV}$, located in single pixels, in time bins of 50 (100) seconds in the PN (MOS) camera(s). Due to variations in the baseline raw cosmic ray rate experienced through the mission to date (probably due to modulation by the solar activity and/or the seasonal variation of satellite apogee direction), we prefer not filter at fixed background count rates, rather for each exposure we define $\pm 3\sigma$ limits after ignoring the highest count rate periods (Figure 2 and 3). Table 2 summarizes the total on-axis *Good Time Interval* (GTI) exposure times extracted for each observation using this procedure.

For clusters RXJ1354.2–0222 and RXJ1701.3+6414 the high prevalence of proton flares mitigated against the automated filtering procedure, and a manual analysis of the “curve of growth” for signal:noise in the cluster target region was employed.

3.2. Vignetting

The clusters in our sample are expected to be extended on a scale of $2\text{--}3 \text{ arc-minutes}$, and in order to assess accurately the surface brightness distribution, a small correction for energy dependent telescope vignetting must be applied. This was performed by the SAS task *EVIGWEIGHT* which assigns a

Cluster ID	RA	Dec	z	Date	Obs ID	Duration	Filter
RXJ0337.7–2522	03:37:45	-25:22:26	0.577 ^s	2001-08-18T11:46:53	0107860401	58942	MEDIUM
RXJ0505.3–2849	05:05:20	-28:49:05	0.509 ^s	2001-09-01T13:17:36	0111160201	48867	THIN
RXJ0847.2+3449	08:47:11	+34:49:16	0.560 ^v	2001-10-07T11:55:10	0107860501	81143	THIN
RXJ1120.1+4318	11:20:07	+43:18:05	0.600 ^b	2001-05-08T20:50:37	0107860201	22627	THIN
RXJ1325.5–3826	13:25:20	-38:24:55	0.445 ^s	2002-01-19T02:30:04	0110890101	60894	MEDIUM
RXJ1334.3+5030	13:34:20	+50:30:54	0.620 ^b	2001-06-07T20:19:43	0111160101	47614	THIN
RXJ1354.2–0222	13:54:17	-02:21:46	0.551 ^s	2002-07-19T15:16:53	0112250101	33374	THIN
RXJ1701.3+6414	17:01:23	+64:14:08	0.453 ^b	2002-05-31T17:49:42	0107860301	18172	MEDIUM

Table 1. Summary of pointing directions for each observation, the overall scheduled durations, and redshift data (^s Southern SHARC, Burke et al., 2003; ^b Bright SHARC, Romer et al., 2000; ^v 160SD Vikhlinin et al., 1998).

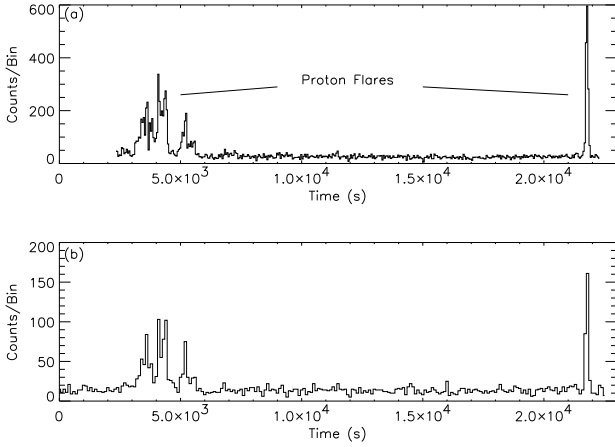


Fig. 2. Count rate in PN (top) and MOS (bottom) cameras in the RXJ1120.1 observation after selection for single pixel events above 10keV. Typical rates ~ 15 cts/50 sec bin (PN) and ~ 8 cts/100 sec bin (MOS)

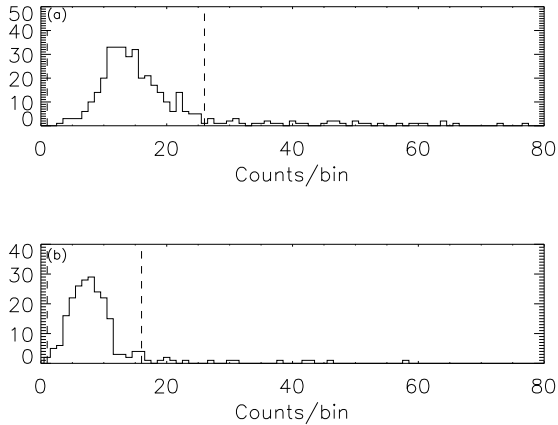


Fig. 3. Histogram of the count rate sequence for PN (top) and MOS (bottom) cameras in the RXJ1120.1 observation after selection for single pixel events above 10keV. The dashed lines indicate the upper and lower ($\pm 3\sigma$) bounds used for the *Good Time Interval* filtering.

Cluster ID	MOS	PN	% lost
RXJ0337.7–2522	23421	23611	60
RXJ0505.3–2849	31851	24983	35
RXJ0847.2+3449	43793	-	50
RXJ1120.1+4318	18333	16208	18
RXJ1325.5–3826	-	48753	20
RXJ1334.3+5030	40713	34909	15
RXJ1354.2–0222	9090	7248	73
RXJ1701.3+6414	9379	4382	50

Table 2. Summary of the usable exposure durations obtained for the different clusters after accounting for the GTI filtering, telemetry losses etc.. In some observations data from only one camera was available. For operational reasons the PN camera commences exposures somewhat later than the MOS cameras. Losses due to proton flares, telemetry drops etc. are given in column 4 as a percentage of the total exposure time.

weighting value to each detected photon, accounting for telescope and CCD efficiency variations (the latter being negligible by comparison). Thereafter, spectrum extraction and image product generation is automatically weighted for the vignetting correction, and response matrices for the on-axis location can be used.¹

An exposure map was also generated for each camera observation. These maps accounted for spatial variations, such as dead pixels, noisy readout columns and chip gaps, not included in the vignetting correction. The XMM-Newton satellite is usually very stable during observations, so the inter-CCD gaps remain approximately fixed in sky projection. It is therefore important to correct for flux lost from extended cluster regions using the exposure maps. This is especially true for the PN images, because the PN CCDs are smaller and the gaps closer to the target than those in the MOS cameras.

3.3. Background subtraction techniques

Background subtraction is a very important step in our analysis. Even after the proton flare removal described above (sec-

¹ In principle this may not apply correctly for objects *far* from the CCD array centre, as the detector response redistribution matrices may diverge slightly from the on-axis case. It is probably also true that mirror vignetting calibrations become less secure with increasing off-axis angle.

tion 3.1), and after masking out point sources, our cluster observations will be contaminated, to varying degrees, by three different background signals; (i) the cosmic X-ray background, (ii) a particle background induced by incident cosmic rays and (iii) some residual soft proton contamination. We will refer to these as the cosmic, particle and proton backgrounds respectively, hereafter. There are two approaches to background subtraction, either one can use the source observation itself (this is known as *in-field* subtraction), or one can use background template files. The templates are generated by combining several deep, blank field, observations and are especially useful when the source of interest covers a large fraction of the field of view (e.g. a nearby cluster). We have used a combination of both techniques in the analysis below.

For each of the eight clusters in our study, we applied the same rate filtering, vignetting correction and detector-to-sky conversion used for the reduction of the cluster observation, to the background template files provided by the XMM-SOC (Lumb et al., 2002). This allowed us to extract identical *physical* detector regions for both the cluster and the background using the SAS task *ATTCALC*. We then re-normalized the background template to account for any differences in the particle background count rates between the cluster and background template observations. This step was necessary because the particle background varies with observation epoch (Section 3.3.1). To make this correction, we took advantage of the fact that high energy particles are not focused by the telescope optics, so the particle background count rate can be measured from areas *outside* the telescope FOV.

We used re-normalized background templates (energy range 0.3–4.5 keV) during the spatial analysis (Section 3.5). We also used background templates (energy range 0.3–10 keV) during the spectral analysis of two of our two brightest clusters (RXJ1120.1 and RXJ1334.3). For this, we employed the so-called “double subtraction” technique (Arnaud et al., 2001), which involves making an additional correction to compensate for the fact that the Galactic Halo and the Local Hot Bubble component of the diffuse cosmic X-ray background varies significantly across the sky. To determine this correction, we compared off-axis, source free, regions in both the cluster fields and their corresponding background templates. We found the correction to be small, due to the lack of soft X-ray emission features at the high Galactic latitude locations of RXJ1120.1 and RXJ1334.3. We have used the results from the double subtraction analysis of RXJ1120.1 and RXJ1334.3 to validate the results from the in-field background subtraction, see below.

For a variety of reasons, e.g. the choice of filter², low signal to noise, non-zero off-axis angle etc., we were not able to apply the double subtraction technique to all our clusters. Instead we have to rely on the in-field technique. The radial dependence of the vignetting means that this technique is most successful for point sources, however it should still work well for our clusters since, at $z > 0.4$, they are barely more extended than the instrument point spread function (PSF). We illustrate this by consid-

ering a cluster described by a β -model with $\beta \sim 0.67$ and a core radius of $25''$ ($\sim 185h_{50}^{-1}$ kpc typical values for the clusters in our sample, Table 5). At a radius enclosing 75% of the counts from such a cluster, the vignetting is different by less than 1% from the aim-point value. Therefore we posit that an accurate representation of the cosmic X-ray background spectrum at the cluster position can be derived using a nearby in-field background aperture. For the spectral analysis of our clusters we generally used an annular background aperture centered on the source. The annuli were chosen on a case by case basis, but were typically $2 - 3'$ wide with an inner radius no less than $3'$ from the cluster center (to ensure that no flux from outlying regions of the cluster was erroneously removed). We note that in the case of RXJ1325.5, we could not use an annulus, due to the proximity of a very bright point source (Section 4.6). In Sections 4.1 and 4.2, we compare the results of the spectral fitting for the clusters where both in field and double subtraction could be applied. As we did not find significant differences, we conclude that the in field background subtraction technique should be valid for our sample.

3.3.1. Impact of Residual Proton Contamination

The ratio of the proton to particle backgrounds is not constant; even after proton flare mitigation (section 3.1), the proton background may have a significantly different counting rate in the cluster observation compared to background template files (Markevitch, 2002). This is illustrated in Figure 4. The triangles indicate the ratio of the particle background in the cluster observation to that in the background template file (column 2 in Table 3). The squares show the equivalent information for the proton background (column 3 in Table 3). For this comparison, the particle background was estimated from the ≥ 10 keV count rate in CCD areas *outside* the telescope FOV, whereas the proton background was estimated by subtracting that value from the ≥ 10 keV count rate within the FOV. From the Figure 4, it is clear that the proton background varies with epoch and is anti-correlated with the particle background. This anti-correlation can be explained if

- enhanced solar activity deposits more protons into the magnetosphere, expanding the latter and thus shielding the cosmic ray flux more efficiently.
- seasonal variations in orbit take the spacecraft in and out of the magnetosphere at apogee, so that cosmic ray flux shielding varies inversely with the exposure to magnetospheric protons.

Although this anti-correlation tends to maintain a more constant *total* background rate, the result of this anti-correlation is that we cannot be certain the background template re-normalizations described above, compensate correctly for the temporal variations in the proton background. This suggests that the in-field background subtraction method may be preferable to double subtraction technique for *spectral* analysis. However, the in-field technique is complicated by the fact that the scattering of low energy protons at the mirrors occurs over angles somewhat larger than for the X-ray reflection (Rasmussen et al., 1999). Therefore, when using task

² The Lumb et al., 2002 background templates are only appropriate for observations made using the Thin filter; three of our clusters were observed through the Medium filter (Table 1)

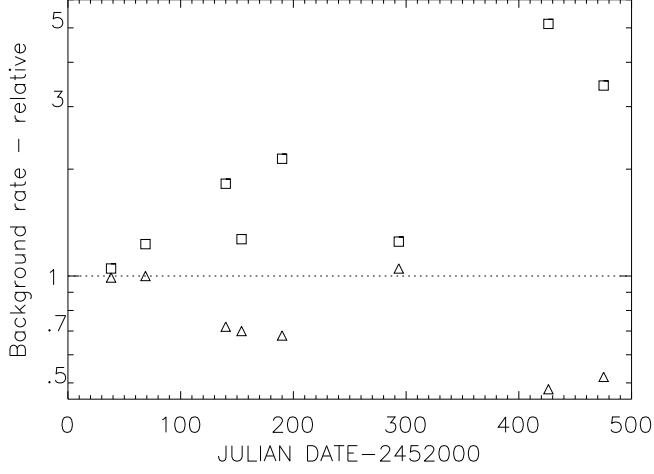


Fig. 4. Comparison of the relative scaling of particle (triangle) and proton (square) background rates (*after GTI filtering*) in the eight cluster observations, with respect to the components of the background template files. Data averaged for all cameras in observation.

EVIGWEIGHT (Section 3.2), there is the potential to over-weight the proton background. The proton background spectrum is hard, so this over-weighting could result in an artificial softening of the cluster spectrum and hence a lowering the estimated cluster temperature, which might in turn mimic evolution in the measured $L_x - T_x$ relation (see section 5.1).

To examine the likely impact of systematic errors in the proton vignetting correction, we used the *EVIGWEIGHT* vignetting corrected background template files to create an image that was essentially free from proton contamination. We did so by applying very strict count-rate filtering. We then made a comparison image by applying less conservative count-rate filtering to the background template files. For this we used the filtering criteria derived from the RXJ1701.3 observation (which suffered from unusually high proton contamination); the comparison is presented in Figure 5. The two count rate images we derived, should be identical within the noise, except with regard to the proton background. By dividing one by the other, and then fitting a radial surface brightness profile, we should therefore be able to get an impression of how the proton background is vignetted. The results of this test (in the 0.5–7.0 keV band to emphasize an effect of hard proton spectrum) are shown in Figure 5. We also generated the equivalent figure using the RXJ1354.2 filtering criteria with almost identical results. From this investigation, we conclude that the proton background is over-weighted by only a few percent by *EVIGWEIGHT* even at the edges of the field of view in observations with significant proton contamination. We therefore chose to ignore the over-weighting of the proton background in our analysis, except in the cases of RXJ1701.3 and RXJ1354.2. For these, we

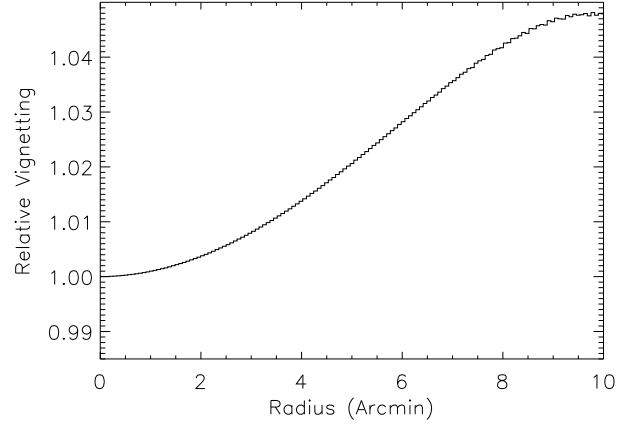


Fig. 5. Ratio of the surface brightness distributions in blank fields, showing proton contamination in RXJ1701.3+6414 field.

Cluster ID	Outside FOV	Inside FOV
RXJ0337.7 – 2522	0.72	1.82
RXJ0505.3 – 2849	0.70	1.27
RXJ0847.2 + 3449	0.68	2.14
RXJ1120.1 + 4318	0.99	1.05
RXJ1325.5 – 3826	1.05	
RXJ1334.3 + 5030	1.00	1.23
RXJ1354.2 – 0222	0.52	3.44
RXJ1701.3 + 6414	0.48	5.13

Table 3. The scaling ratio of the > 10 keV count rates outside (column 2) and inside (column 3) the telescope FOV in the background template files compared to the cluster files. The former ratio is an indication of the particle (cosmic ray) background rate, while the latter indicates the level of the soft proton background rate. These ratios are plotted as a function of Julian date in Figure 4

applied a small ($\sim 2\%$) scaling to the background spectrum derived from an in-field annulus around the cluster.³

3.4. Image Products

Images for each camera were compiled in the 0.3–4.5 keV energy band, this maximizes source count rates for cluster spectra that are characterized by a ~ 4 keV temperature, and furthermore provides a guard against corrections at the softest and hardest energy bands that are subject to the largest potential Galactic and cosmic ray subtraction inaccuracy. A spatial binning of 4.3 arc-seconds per pixel, was employed, which slightly oversamples the mirror FWHM. The 3 separate count-rate images from the EPIC cameras were exposure corrected and co-added. In each image field, we use the SAS task *EBOXDETECT* to identify point sources via a sliding box de-

³ We caution the reader not to use Figure 5 as a general template for XMM-Newton analysis, as both the spectrum and the absolute count rate of the proton background are likely time dependent.

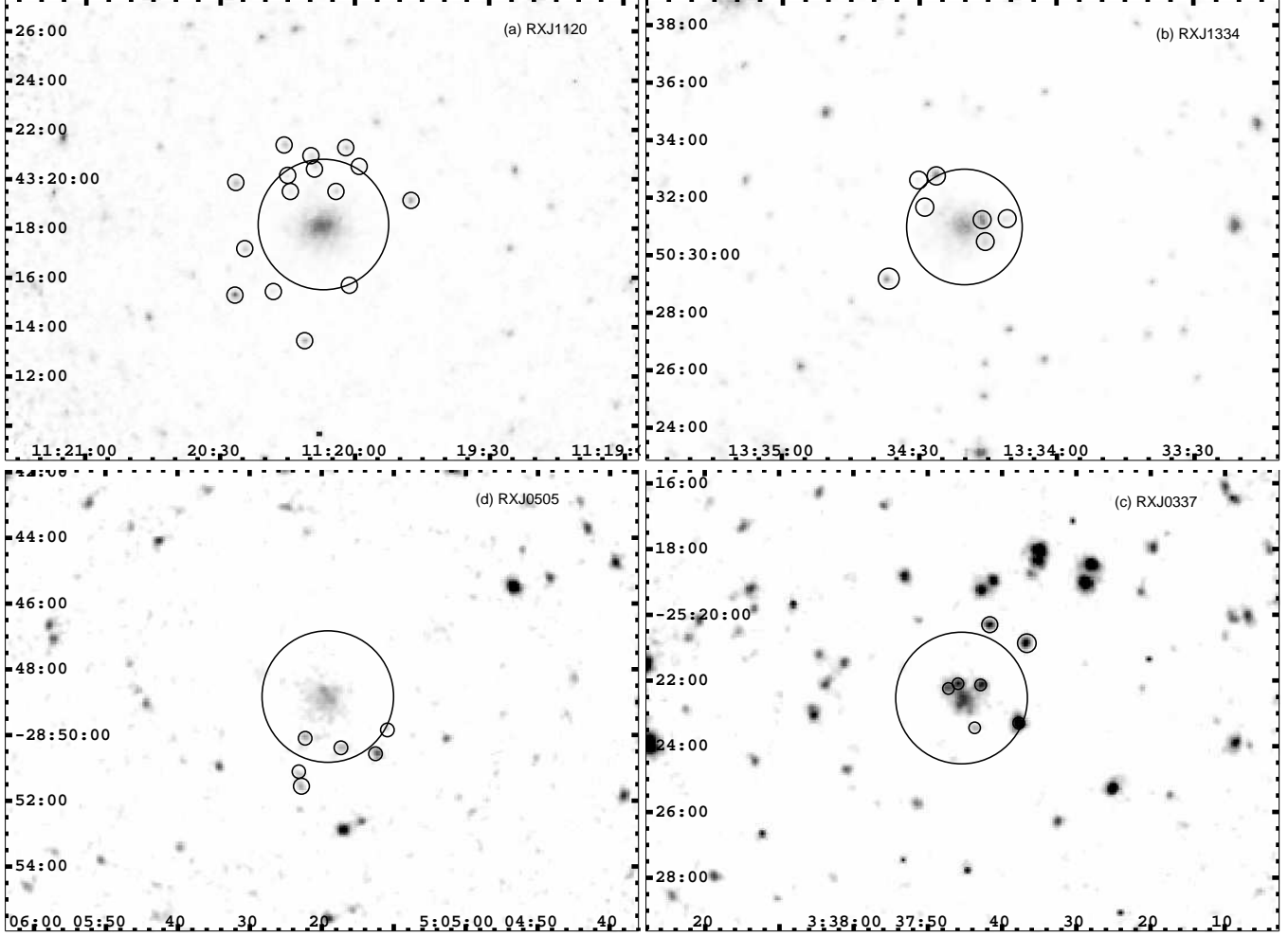


Fig. 6. (a) Central $\sim 18 \times 18$ arc-minutes of the RXJ1120.1 field - smoothed by a $4''\sigma$ Gaussian. The large circle represents the spectral extraction radius, and the smaller circles locate the point sources which were excised. Similar images for RXJ1334.3 (b), RXJ0337.7 (c) and RXJ0505.3 (d). The RXJ1334.3 image 15×15 arc-minutes; the RXJ0337.7 and RXJ0505.3 images are 14×14 arc-minutes.

tection algorithm (see Table A.1). In Figures 6 and 7, we show the inner portion of the eight cluster images after a Gaussian smoothing of $\sim 4''$ (using the *FTOOL fgauss*). It is clear from these images that the clusters are well resolved and encompass a variety of morphologies. Point sources masked during the spatial and spectral analysis (section 4) are indicated by small circles. The larger circles denote the apertures used to generate the cluster spectrum.

3.5. Radial surface brightness profiles

Before generating the profile, we defined the centroid of the cluster brightness distribution using a 2-d Gaussian fit around the core of the raw cluster image (0.3–4.5 keV). These centroids are given in Table 5, row 1. Next, a background correction was applied by subtracting, pixel by pixel, the corresponding re-normalized background template (Section 3.3). The radial bins were chosen so that the background-subtracted counts per bin, in the co-added profile, were at $\geq 3\sigma$ significance.

A β -model convolved with the XMM-Newton telescope PSF appropriate at the position of the cluster centroid was then fit to these profiles, using simple χ^2 -minimization (background was fixed). For the PSF convolution, we used calibration file XRTn_XPSF_0004.CCF in SAS medium accuracy mode, available from the XMM-SOC calibration ftp site. The PSF was constructed by co-adding the contribution from PSFs at different energies using a weighting scheme appropriate for a 4keV thermal spectrum. Fortunately the XMM-Newton telescope PSF is a rather weak function of X-ray energy, so that any deviations from this default spectrum would have a negligible impact on our fits. We were able to use the on-axis PSF for the convolution, except in the case of RXJ1325.5. For this cluster, which was observed off-axis, the appropriate off-axis PSF model was generated. We note that the PSF correction was applied separately for each camera. Fitted values for β and the core radius r_c are given in Table 5 rows 8 & 9. To convert the core radii from angles to distances for this Table, we assumed a spatially flat cosmology with $\Omega_M = 1$

and $H_0 = 50 \text{ km s}^{-1} \text{ Mpc}^{-1}$. The eight radial profiles and their respective best fit PSF convolved β models are presented in Figures 19 and 20.

3.6. Spectral extraction

Cluster spectra were extracted from circular regions centred on the cluster centroids, with radii ranging from 90 to 145 arcseconds (typically $120''$, see Table 5, row 13). From these regions we extracted data from the event list using the recommended pixel selections. For the PN camera we used single and double pixel events (event patterns 0–4) with all the recommended selection flags applied. For the MOS cameras, we used the 0–12 event patterns. We account for background contamination in the spectra using either the double and/or in-field subtraction methods (Section 3.3).

Spectral fitting was implemented with the XSPEC v11 package (Arnaud, 1996), using the MEKAL models (Mewe et al., 1986) for a thermal spectrum, modified with interstellar absorption (McCammon & Sanders, 1990) appropriate for the Galactic column density (Dickey & Lockman, 1990). To facilitate fitting via Chi-square minimization, the spectral files were re-binned to ensure at least 25 counts per bin in order to approximate Gaussian statistics. The energy range was 0.3–10 keV. In general, the following on-axis response files were used during the fits, *epn_ff20_sdY9_filter.rmf* for the PN camera and *m1(2)_filterv9q20t5r6_all_15.rsp* for the MOS1(2) cameras. Exceptions to this, e.g. during the analysis of RXJ1325.5, are noted below. Fitted spectral parameters are quoted with 1σ confidence limits on one interesting parameter. The spectral fits were typically performed simultaneously on the PN, MOS1(2) spectra. Again exceptions to this, e.g. during the analysis of RXJ0847.2, are noted in the relevant sections.

Following Markevitch (1998), we have also investigated the impact of cooling cores on our fitted temperatures, and hence the measured $L_x - T_x$ relation, by performing spectral fits after excising the central region. For all clusters except RXJ1701 and RXJ1325, a $50 h_{50}^{-1} \text{ kpc}$ region was excised. For RXJ1701 & 1325 a 120 kpc region was excised (see section 4.7). The results from these fits are given at the beginning of Table 5. See Section 5.2.1 for a discussion.

3.7. Deriving Bolometric Luminosities

For the luminosity calculations, we adopted a physically meaningful circular aperture, with a virial radius, r_v . We derived r_v according to the $T - r_v$ relation of Evrard et al. (1996) for each cluster using the best fit temperatures from the spectral fits. We note that uncertainties both in the measured temperature and in the $T - r_v$ relation will introduce a systematic error in the derived L_x values. However, this should be insignificant, as very little cluster flux falls at radii close to the virial radius.

We integrated the background-subtracted counts inside r_v and then corrected for any cluster flux lost in areas under masked point sources or inter-chip gaps. The correction factors are given in row 12 of Table 5. These were derived in a model

independent fashion; the count-rate was accumulated in 1 pixel wide annuli centered on the cluster. If any pixels within a specific annulus fell in chip gaps or in the point source masked, the annulus count-rate was scaled up accordingly. Next, we used XSPEC, together with the appropriate EPIC response functions, to determine the absorbed 0.3–4.5 keV flux within r_v , using the best fit absorbed MEKAL model from our spectral analysis so that it yielded the measured $r < r_v$ count rate (the MEKAL normalization factors are given in row 10 of Table 5). For comparison with equivalent ROSAT data such as SHARC or 160SD these fluxes (converted to the normal ROSAT 0.5–2 keV band) are listed in row 6 of Table 5. We then set the hydrogen column density to zero and re-determined the flux inside a pseudo bolometric band of 0.0–20 keV. From the unabsorbed bolometric flux, it is trivial to determine the bolometric luminosity for any given cosmological model. To aid comparisons with previous work, we give in, row 3 of Table 5, the L_x values appropriate for a $\Omega_M = 1$, $\Omega_\Lambda = 0$, $q_0 = 0.5$ model with $H_0 = 50 \text{ km s}^{-1} \text{ Mpc}^{-1}$ that has been most frequently used in the past as the parameter set for X-ray cluster studies.

Also following Markevitch (1998), we estimated the cooling flow corrected bolometric luminosities by summing counts in a ($r_{\min} \leq r \leq r_v$) ring. For clusters other than RXJ1701 and RXJ1325, $r_{\min} = 50 h_{50}^{-1} \text{ kpc}$, while for RXJ1701&1325 $r_{\min} = 120 h_{50}^{-1} \text{ kpc}$ (see section 4.7). To account for the non-cooling flow flux falling at $r \leq r_{\min}$, we applied a cluster specific renormalisation parameter calculated using the best fit β -model. We note that our correction approach differs from that of Markevitch (1998), therein a single multiplicative factor of 1.06 was used.

4. Individual Clusters

We now discuss our analysis for each cluster in turn. We have ordered our discussion according to the Julian date on which they were observed (Table 1).

4.1. RXJ1120.1+4318

Figure 6(a) shows the vignetting corrected, background subtracted and co-added (PN+MOS1+MOS2) 0.3–4.5 keV image of RXJ1120.1+4318. Point sources removed during analysis are circled and their positions listed in Table A.1. Figure 19 shows the corresponding radial surface brightness distribution and best fit β model; $\beta = 0.77 \pm 0.03$, $\theta_c = 27.4 \pm 1.2$ arcseconds ($r_c = 209^{+9}_{-8} h_{50}^{-1} \text{ kpc}$, Table 5).

From a spectral extraction region with a radius of $145''$ and using the in-field background subtraction technique, we measured the following temperature, metal abundance and redshift by fitting to the PN, MOS1 and MOS2 data simultaneously; $T_x = 5.45^{+0.26}_{-0.35} \text{ keV}$, $Z = 0.47 \pm 0.09$, $z = 0.60 \pm 0.08$. We note the consistency between the redshift measured from the X-ray spectrum with the optically determined value ($z = 0.60$; Romer et al. 2000). The overall χ_ν of the spectral fit was 390 / 360 degrees of freedom. During the fit, the hydrogen column density was fixed at the Galactic value ($N_H = 2.1 \times 10^{20} \text{ atoms cm}^{-2}$), but we note that, when left as a free parameter, its best fit value was very similar ($N_H = 2.2 \pm 0.4 \times 10^{20} \text{ atoms cm}^{-2}$).

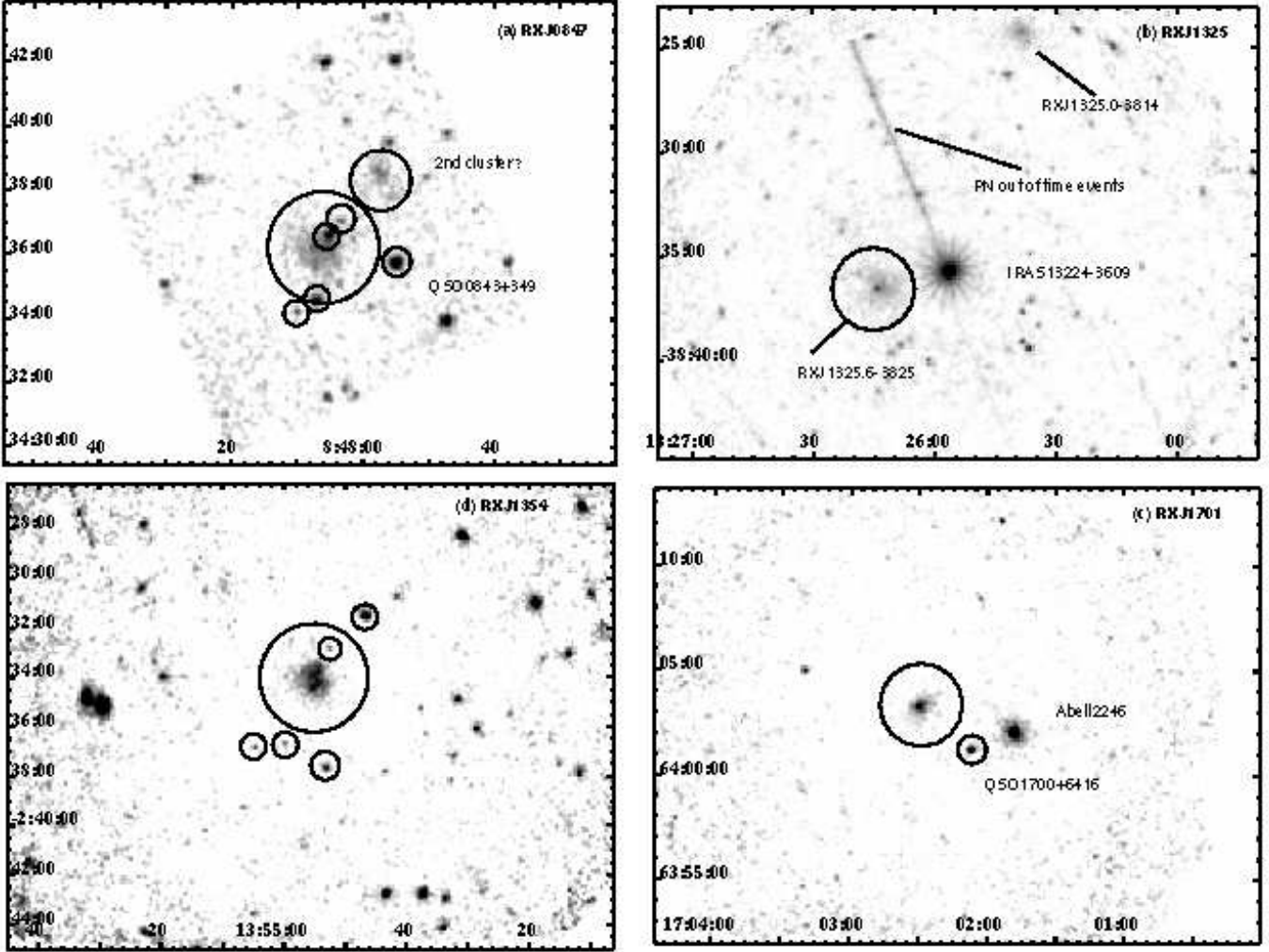


Fig. 7. (a) Central MOS CCD image (10 arc-min) of the RXJ0847.2 field - smoothed by a $4''$ Gaussian. The large circle represents the spectral extraction radius, and the smaller circles locate the point sources which were excised. Similar images for RXJ1325.5 (b), RXJ1701.3 (c) and RXJ1354.2 (d). A newly discovered candidate distant cluster (XMMU J084701.8+345117) is labeled to the upper right of RXJ0847.2. The RXJ1325.5 and RXJ1325.0 Southern SHARC clusters fall in an observation centered on IRAS 13224-3809. The long streak connected to IRAS 13224-3809 comes from the “out-of-time” events collected during readout of the PN camera. In the RXJ1701.3 field, the nearby Abell 2246 and QSO objects are labeled. The RXJ1325.5 image is $\sim 18 \times 18$ arcminutes; the RXJ1701.3 and RXJ1354.2 images are $\sim 14 \times 14$ arcminutes.

Of the eight clusters in our sample, this object has the greatest signal-to-noise ratio. We have taken advantage of this to perform additional spectral analyses. First we have been able to use the double subtraction technique to investigate how the adopted background subtraction method impacts the spectral fits. Doing so, we derive $T_x = 5.6^{+0.25}_{-0.3}$ keV, $Z = 0.43 \pm 0.06$, $z = 0.605 \pm 0.08$ (Figure 8). The overall χ_ν of the spectral fit was 330 / 307 degrees of freedom. During the fit, the hydrogen column density was again fixed at the Galactic value ($N_H = 2.1 \times 10^{20}$ atoms cm^{-2}), but when left as a free parameter, its best fit value was ($N_H = 2.2^{+0.2}_{-0.4} \times 10^{20}$ atoms cm^{-2}). It is clear, therefore, that the spectral fits are not significantly changed by the choice of background subtraction technique (see also section 4.2).

We have also investigated how the spectral fits differ when we treat the PN and MOS data separately. We find them to be in good agreement; $T_{x,\text{PN}} = 5.30 \pm 0.6$ keV and $T_{x,\text{MOS}} = 5.7 \pm 0.8$ keV. This is encouraging since, in two other cases (RXJ1325.5 and RXJ0847.2), we do not have access to data from all three cameras. We have also been able to subdivide the spectral extraction region into three radial bins, and determined a crude temperature profile (Figure 9). The profile is essentially flat, indicating that there is not a “cooling flow” region at the cluster core (this conclusion is supported by the absence of a central spike in the surface brightness profile). We note that for the PN/MOS comparison and for the radial profile, we used the double subtraction technique to account for the background.

T_{mean}	EdS L_x ($10^{44} \text{ erg s}^{-1}$)	β	θ_c (")
$5.3 \pm 0.5 \text{ keV}$	13.9 ± 0.8	$0.78^{+0.06}_{-0.04}$	$26.4^{+3.6}_{-2.4}$
$5.6^{+0.25}_{-0.3} \text{ keV}$	14.4 ± 0.2	0.77 ± 0.03	27.4 ± 1.2

Table 4. Comparison of parameter fits to the RXJ1120.1 observation by Arnaud et al. (2002) (first line) and this work (second line). Here L_x refers to the bolometric luminosity.

4.1.1. Comparison with Arnaud et al. 2002

The RXJ1120.1 observation described here have been previously analyzed and interpreted in an earlier paper in this series (Arnaud et al., 2002). The analysis procedures developed in that paper have formed the basis of the analysis of the eight clusters described here. For example, the vignetting correction technique used in Arnaud et al. (2002) has been subsequently implemented in SAS as the *EVIGWEIGHT* routine mentioned above. However, there are certain differences in our respective data analysis techniques, even with regard to the RXJ1120.1 observation. For example, we use updated calibration information and an updated SAS processing version. We also used a different method (3-sigma clipping) for the GTI filtering. We have also adopted the in-field background subtraction method as the standard for our cluster analysis (in Arnaud et al. (2002), only the double subtraction technique was used). Finally, we note our use of the both single and double PN events, compared to the selection of single events by Arnaud et al. (2002). In general the revised analysis of RXJ1120.1 has yielded very similar results to Arnaud et al. (2002) and we concur that, given its isothermal temperature profile and the absence of significant substructure, RXJ1120.1 is consistent with being a relaxed cluster. It is noteworthy, however, that in Arnaud et al. (2002) the mean temperature values determined using only MOS data differed from those determined using only PN data by more than 1 keV; $T_{x,MOS} = 5.8^{+1.0}_{-0.7} \text{ keV}$ and $T_{x,PN} = 4.5^{+0.8}_{-0.5} \text{ keV}$. By contrast, we measured temperatures that differed by only 8% (see above). This improvement is most likely attributable to the improved calibration that has become available since Arnaud et al. (2002) was published. For completeness we compare in Table 4 the values derived for various fitted parameters in the two analyses. For consistency with Arnaud et al. (2002), we quote the mean temperature derived using the double subtraction technique (in Table 5 we quote the value from based on the in field subtraction technique).

4.2. RXJ1334.3+5030

Figure 6(b) shows the image of the RXJ1334.3+5030 field. Point sources removed during analysis are circled and their positions listed in Table A.1. Figure 19 shows the corresponding radial surface brightness distribution and best fit β model; $\beta = 0.66 \pm 0.02$, $\theta_c = 20 \pm 1 \text{ arcseconds}$ ($r_c = 154 \pm 10 h_{50}^{-1} \text{ kpc}$, Table 5).

From a spectral extraction region with a radius of $120''$ and using the in-field background subtraction technique, we measured the following temperature and metal abundance; $T_x = 5.20^{+0.26}_{-0.28} \text{ keV}$, $Z = 0.15 \pm 0.08$ (Figure 10). The overall χ_ν of

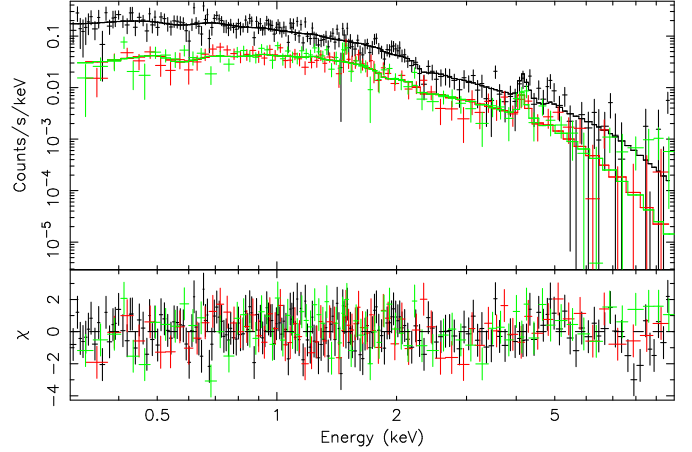


Fig. 8. Spectral fit and residuals for RXJ1120.1; black - PN, dark and light grey - MOS1&2 (double background subtraction).

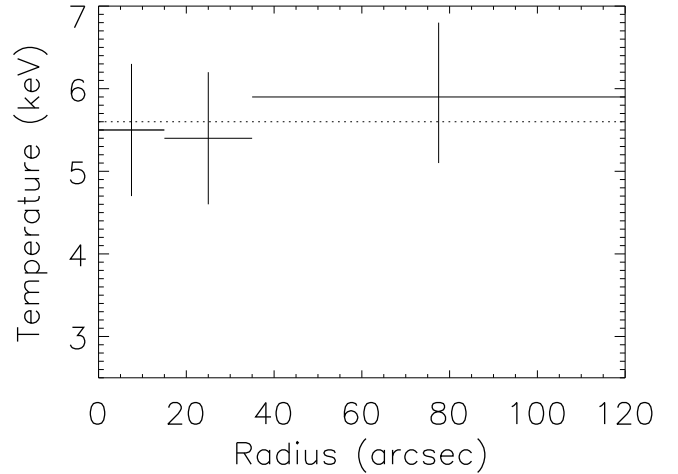


Fig. 9. The spatially resolved temperature profile of RXJ1120

the spectral fit was 464 / 473 degrees of freedom. The hydrogen column was fixed at the Galactic value ($N_H = 1.05 \times 10^{20} \text{ atoms cm}^{-2}$), but we note that, when left as a free parameter, its best fit value was very similar ($N_H = 0.8 \pm 0.5 \times 10^{20} \text{ atoms cm}^{-2}$). Likewise, the redshift was fixed at its optically derived value of $z = 0.62$ (Romer et al. 2000), but when left as a free parameter, its best fit value was 0.63 ± 0.02 . The derived values for the bolometric luminosity and absorbed flux inside the virial radius are given in Table 5. We were also able to apply the double subtraction technique to these data and derived a consistent mean temperature value; $T_x = 5.05 \pm 0.3 \text{ keV}$.

4.3. RXJ0337.7-2522

Figure 6(c) shows the vignetting corrected, background subtracted image of the RXJ0337.7-2522 field. Two excised sources within the spectral extraction radius, XMMU J033742.9-252208 & XMMU J033745.9-252206, are ten-

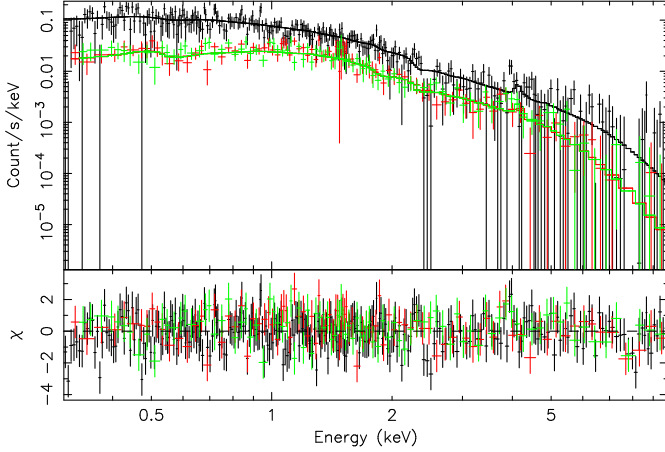


Fig. 10. Spectral fit and residuals for RXJ1334.3; black - PN, dark & light gray - MOS1&2 (in-field background subtraction).

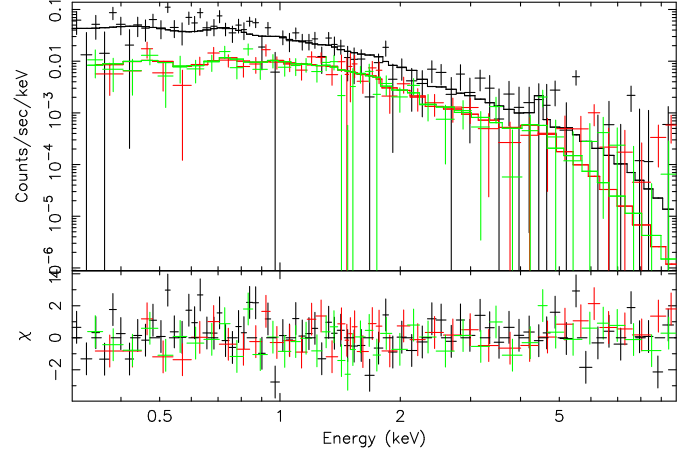


Fig. 12. Spectral fit and residuals for RXJ0505.3; black - PN, dark & light gray - MOS

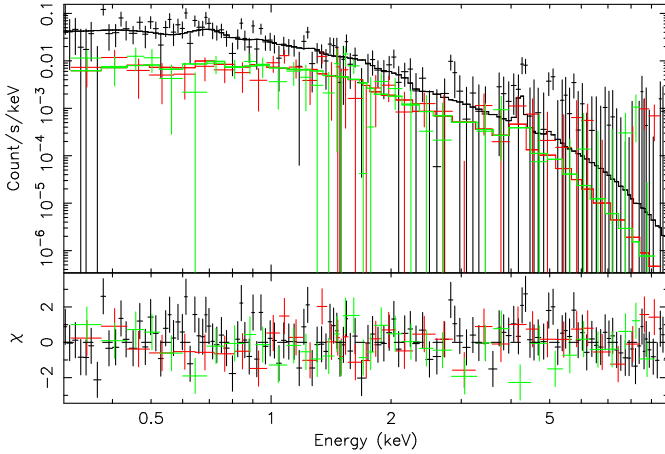


Fig. 11. Spectral fit and residuals for RXJ0337.7; black - PN, dark&light gray - MOS1&2

tatively associated with two stellar objects on the USNO Catalogue. The former is U0600-01432100, also identified as blue stellar object PHL4470, the latter is identified as U0600-01432383 (a 16.5 r magnitude object). Figure 19 shows the radial surface brightness distribution and best fit β model; $\beta=0.76^{+0.08}_{-0.04}$ and $r_c=19.4 \pm 2.5$ arcseconds. ($r_c = 145 \pm 18 h_{50}^{-1}$ kpc, Table 5).

From a spectral extraction region with a radius of $120''$ and using the in-field background subtraction technique, we measured the following temperature, metal abundance and redshift; $T_x = 2.6 \pm 0.35$ keV, $Z = 0.38 \pm 0.09$, $z = 0.57 \pm 0.3$ (Figure 11). The overall χ_ν of the spectral fit was 193 / 214 degrees of freedom. We note the consistency between the redshift measured from the X-ray spectrum with the optically determined value ($z = 0.577$; Burke et al., 2003). The hydrogen column density was fixed at the Galactic value ($N_H = 0.99 \times 10^{20}$ atoms cm^{-2}), when left as a free parameter, its best fit value was very similar ($N_H = 8.7^{+6.4}_{-5.4} \times 10^{19}$ atoms cm^{-2}). The derived values for the

bolometric luminosity and absorbed flux inside the viral radius are given in Table 5.

4.4. RXJ0505.3-2849

The RXJ0505.3-2849 field is shown in Figure 6(d). Four point sources removed during analysis are circled and their positions listed in Table A.1. Tentative identifications of these sources with objects in the UK APM survey (Maddox et al., 1990) suggest an absolute astrometric accuracy for our observations of ~ 2 arcseconds. Figure 19 shows the corresponding radial surface brightness distribution and best fit β model; $\beta=0.66^{+0.05}_{-0.04}$ and $r_c=22.8 \pm 2.4$ arcseconds. ($r_c = 164 \pm 17 h_{50}^{-1}$ kpc, Table 5).

From a spectral extraction region with a radius of $120''$ and using the in-field background subtraction technique, we measured; $T_x = 2.5 \pm 0.3$ keV, $Z = 0.17 \pm 0.08$ (Figure 12). The overall χ_ν of the spectral fit was 279 / 248 degrees of freedom. The fixed Galactic hydrogen value was $N_H = 1.5 \times 10^{20}$ atoms cm^{-2} , compared with a free fit parameter, of $N_H = 1.1 \pm 0.6 \times 10^{20}$ atoms cm^{-2} . The redshift was fixed at its optically derived value of $z = 0.51$ (Burke et al., 2003), but when left as a free parameter, its best fit value was $z = 0.53 \pm 0.04$. As a test, we have also performed a spectral fit without excluding the four point sources. We find that, within the errors, the fitted temperature was unchanged.

4.5. RXJ0847.2+3449 (and XMMU J084701.8+345117)

Figure 7(a) shows the image of RXJ0847.2+3449. Of the eight clusters in our sample, RXJ0847.2+3449 is noteworthy as being the only one that is not a SHARC cluster; it was selected instead from the 160SD (Vikhlinin et al., 1998). RXJ0847.2 was observed during a period when the PN camera was temporarily disabled by a hardware fault, and the requested exposure duration was partly compensated by an extension of the MOS observation. To improve the contrast of the cluster against the nearby

bright QSO (PG 0844+34), only the inner part of the image, that covering central CCD of the MOS cameras, is shown in Figure 7(a). We note that the mirror scattering is sufficiently low that no flux from PG 0844+34 impedes our analysis. The bright point source ~ 3 arcminutes west of the RXJ0847.2 cluster in Figure 7(a) was identified with a second, fainter, quasar, QSO 0843+349 at $z = 1.57$. The image also shows evidence for a nearby *fainter* extended object to the NW, which we identify as a cluster candidate with provisional designation XMMU J084701.8+345117. Vikhlinin (private communication) claims to have found a concentration of faint galaxies in this region, but to date no galaxy redshifts are available. Neither QSO 0843+349 nor XMMU J084701.8+345117 fall inside our spectral extraction region. The source detection software picked out four sources in that region, none of which have counterparts in the NED catalogs. These sources were excluded from the spatial and spectral analysis, they are circled in Fig. 7 and their positions are listed in Table A.1.

Figure 20 shows the radial surface brightness distribution for RXJ0847.2 and the best fit β model; $\beta=0.81\pm0.07$ and $r_c=42^{+4}_{-4}$ arcseconds. ($r_c = 307 \pm 30 h_{50}^{-1}$ kpc, Table 5). From a spectral extraction region with a radius of $120''$ and using the in-field background subtraction technique, we measured $T_x = 3.62^{+0.58}_{-0.51}$ keV, $Z = 0.30 \pm 0.28$ (Figure 13). The overall χ_ν of the spectral fit was 152 / 180 degrees of freedom. The fixed hydrogen column density was $N_H = 3.2 \times 10^{20}$ atoms cm^{-2} , as a free parameter, its best fit value was $N_H = 2.8 \pm 0.14 \times 10^{20}$ atoms cm^{-2} . The redshift was fixed at its optically derived value of $z = 0.56$ but its best fit value was $z = 0.54 \pm 0.04$. As a test, we have also performed a spectral fit without excluding the four point sources. Doing so changed the fitted temperature by 0.1 keV and the measured flux by $\leq 10\%$.

We have also estimated the temperature of the second cluster in the field, XMMU J084701.8+345117. For this we used a spectral extraction radius of 80 arcsec and the in field background subtraction technique. We do not have an independent estimate of the cluster redshift, and it cannot be constrained by the X-ray spectrum, so we have assumed that the cluster lies at the same redshift as RXJ0847.2 ($z = 0.56$). We have also fixed the metal abundance to be $Z = 0.3$ and the hydrogen column density to the same Galactic value. We measure a cluster temperature of $T_x = 1.8^{+1.0}_{-0.4}$ keV and a corresponding ($r < r_c$, 0.5–2 keV) flux and bolometric luminosity of 1.3×10^{-14} erg cm^{-2} s^{-1} and 1×10^{43} erg s^{-1} respectively. These results are consistent with measured low red-shift $L_x - T_x$ relations.

4.6. RXJ1325.5–3826 (and RXJ1325.0-3814)

The data for this cluster were obtained by kind permission of Guaranteed Time holder M Watson, from an observation of the nearby object IRAS 13224-3809. Unfortunately for our own purposes, this bright source had been observed in the MOS cameras in a “Window” mode of readout on the central CCDs in order to minimize effects of photon pile-up, and consequently the area of focal plane containing the SHARC cluster was not exposed. Therefore, our spatial and spectral analysis is restricted to the PN camera data only. Figure 7(b) shows the

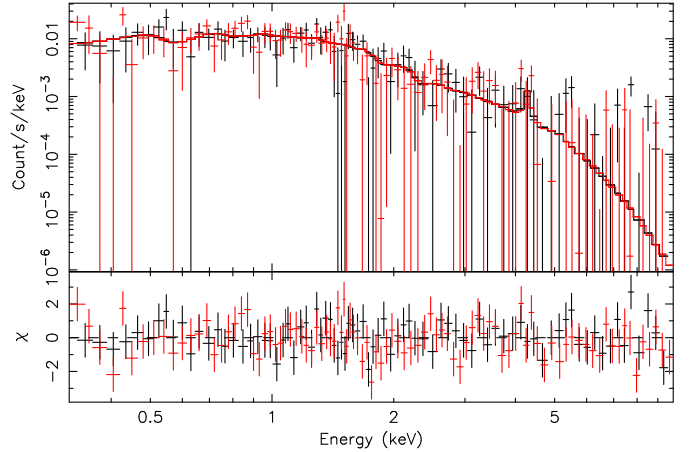


Fig. 13. Spectral fit and residuals for RXJ0847.2 (MOS data only)

vignetting corrected, background subtracted 0.3–4.5 keV PN image of the region surrounding IRAS 13224-3809. Clusters RXJ1325.5–3826 and RXJ1325.0-3814 (see below) are labeled, as is the streak corresponding to the “out of time” events from IRAS 13224-3809. IRAS 13224-3809 is bright enough that the “spider” like structure in the PSF is visible around it. Given the proximity of the cluster to the IRAS source, the surface brightness profile for RXJ1325.5–3826 (Figure 20) was extracted from manually selected clean regions that avoided the IRAS 13224-3809 PSF.

For the β model fitting, a PSF appropriate for the PN at the off-axis angle of the cluster was used (for all the other clusters in our sample, we had used the on-axis PSF). The best fit parameters in the spatial fit are $\beta = 0.64^{+0.09}_{-0.07}$ and $\theta_c = 17.3 \pm 3.0$ arcseconds ($r_c = 115 \pm 20 h_{50}^{-1}$ kpc, Table 5). There is evidence for possible excess brightness in the inner bins of the radial profile. This may be an indication of a central cooling core, but we do not have adequate signal to noise to confirm this spectroscopically. Following the procedure adopted for RXJ1701.3 (see below) we also performed a β fit after exclusion of the core 120 kpc and found a value for β of 0.71 ± 0.05 , given a fixed r_c of $200 h_{50}^{-1}$ kpc (We fixed this value arbitrarily to match typical cluster values).

We used a $90''$ radius extraction region to fit the spectrum from this cluster. This is a smaller region than was used for the other clusters ($120''$ or $145''$, Table 5) because of the proximity of IRAS 13224-3809. Even though the proton background was low enough in this exposure to permit spectral measurements using the double subtraction technique, we decided to use instead only the in-field background subtraction technique. This was because we wanted to mimic the off-axis angle dependence of the point source contamination. Rather than using an annulus around the cluster to determine the background, we used two source and streak free circular regions at the same off-axis angle as the cluster. From the background subtracted PN spectrum, we measured the following temperature, metal abundance and redshift; $T_x = 4.15^{+0.4}_{-0.3}$ keV, $Z = 0.31^{+0.19}_{-0.17}$, $z = 0.44 \pm 0.01$ (Figure 14). We note the consistency between

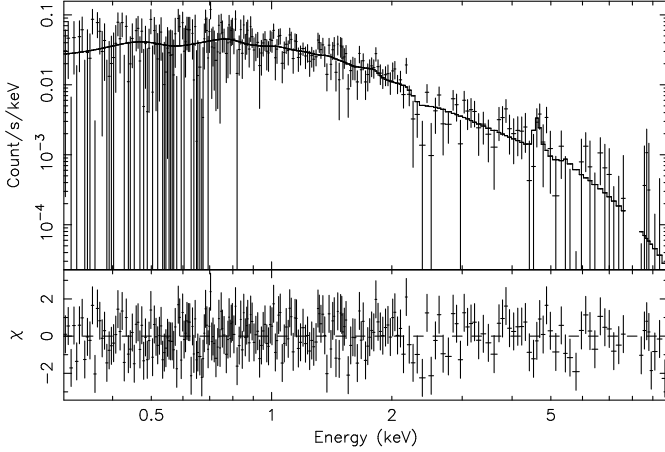


Fig. 14. Spectral fit and residuals for RXJ1325.5 (PN data only)

the redshift measured from the X-ray spectrum with the optically determined value ($z = 0.445$; Burke et al., 2003). The overall χ_ν of the spectral fit was 229 / 242 degrees of freedom. The fixed and free hydrogen column density values were $d(N_H = 4.8 \times 10^{20} \text{ atoms cm}^{-2}$ and $4.5^{+0.9}_{-0.8} \times 10^{20} \text{ atoms cm}^{-2}$ respectively.

4.6.1. RXJ1325.0-3814

For completeness, we note that another, fainter, Southern SHARC cluster lies within the same field of view. The PN image of this cluster, RXJ1325.5-3814, can be seen in Figure 7(b). The cluster is also visible in the MOS data (not shown) because it lies outside the region blanked by the “Window” mode. The cluster is too faint and too far off axis (*i.e. where the PSF is poorly defined*) to permit a detailed spatial analysis, however we were able to make a spectral analysis. For this we generated off-axis response matrices for each camera using the SAS *ARFGEN* package. From a spectral extraction region with a radius of $90''$, and using the in-field background subtraction technique, we measured the following temperature and redshift (N_H fixed at the same galactic value of $4.8 \times 10^{20} \text{ atoms cm}^{-2}$ and abundance at 0.3) $T_x = 3.2 \pm 0.4 \text{ keV}$ and a redshift of $z = 0.29 \pm 0.02$. We note the consistency between the redshift measured from the X-ray spectrum with the optically determined value ($z = 0.296$; Burke et al., 2003).

The cluster is observed close to the edge of the outer CCDs, preventing the use of an extraction region large enough to correspond with the virial radius. Within a radius $\sim 500 h_{50}^{-1} \text{ kpc}$, the measured flux and bolometric luminosity are $6.1 (\pm 0.3) 10^{-14} \text{ erg cm}^{-2} \text{ s}^{-1}$ (0.5–2 keV) and $L_x = 1.1 \pm 0.23 10^{44} \text{ erg s}^{-1}$ respectively. This combination of T_x and L_x are not consistent with the measured $L_x - T_x$ relation for nearby clusters. For example, for $T_x = 3.2 \text{ keV}$, one would expect a bolometric luminosity of $L_x = 2 \times 10^{44} \text{ erg s}^{-1}$ based on the Markevitch (1998) relation, and is probably due mainly to the missing flux outside our spectral extraction radius.

4.7. RXJ1701.3+6414 (and Abell 2246)

This cluster was observed during an exposure scheduled near the end of an orbit, where the spacecraft was approaching the particle belts. Not only were the spacecraft operations terminated prematurely, but most of the exposure was dominated by high soft proton background from the edge of the particle belts. Fortunately this is one of the brightest clusters in our sample and we were still able to produce acceptable quality images and spectra.

Figure 7(c) shows the image of the RXJ1701.3+6414 field. Two nearby sources are marked on the Figure; a QSO (HS1700+6416) and a known cluster (A2246).

The XMM-Newton data indicate an anomalously low r_c value in the β -fit, and this is supported by CHANDRA data (Vikhlinin et al., 2002) where this cluster was observed with a suspected cooling flow central brightness enhancement. We therefore excluded the central bins ($120 h_{50}^{-1} \text{ kpc}$) and fixed the r_c to the CHANDRA value of 0.5 arcmin (204 kpc). Figure 20 shows the corresponding radial surface brightness distribution and resulting best fit β model; $\beta = 0.64 \pm 0.05$, $\theta_c = 30$ arcseconds. This value for β is consistent with the CHANDRA measurement (0.62 ± 0.03).

From a spectral extraction region with a radius of $120''$, we measured the following temperature, metal abundance and redshift (without core excision); $T_x = 4.5^{+1.5}_{-1.0} \text{ keV}$, $Z = 0.24 \pm 0.2$, $z = 0.44 \pm 0.02$ (Figure 15). The overall χ_ν of the spectral fit was 58 / 53 degrees of freedom. The hydrogen column density was fixed at the Galactic value ($N_H = 2.6 \times 10^{20} \text{ atoms cm}^{-2}$), and as a free parameter, its best fit value was very similar ($N_H = 2.6 \pm 1.5 \times 10^{20} \text{ atoms cm}^{-2}$).

After excluding the 120 kpc cooling flow region we obtain $T_x = 4.8^{+1.9}_{-1.3} \text{ keV}$. The derived values for the bolometric luminosity and absorbed flux inside the virial radius are given in Table 5. We were unable to apply the double subtraction technique to these data because of the enhanced proton background during the observation (see Figure 5). The poorer quality of data in this observation limits the quality of determination of T and L. Agreement with the CHANDRA data is acceptable for the temperature, but not the luminosity ($5.8 \pm 0.5 \text{ keV}$ and $15.7 \times 10^{44} \text{ erg/s}$ respectively).

4.7.1. Abell 2246

For completeness we also offer our interpretation of the Abell 2246 spectrum. From a spectral extraction region with a radius of $90''$, and using the in-field background subtraction technique, we measured the following temperature, metal abundance and redshift by fitting to the PN, MOS1 and MOS2 data simultaneously; $T_x = 2.7^{+0.6}_{-0.5} \text{ keV}$, $Z = 0.32 \pm 0.13$, $z = 0.22 \pm 0.04$. We note the consistency between the redshift measured from the X-ray spectrum with the optically determined value ($z = 0.225$; Struble and Rood, 1991). Within a radius $\sim 415 h_{50}^{-1} \text{ kpc}$, the flux and bolometric luminosity are $3.4 \pm 0.2 10^{-13} \text{ erg cm}^{-2} \text{ s}^{-1}$ (0.5–2 keV) and $2.1 10^{44} \text{ erg s}^{-1}$ respectively. Despite the rather restricted radius from which the luminosity is determined, the local $L_x - T_x$ relation would predict a slightly lower luminosity than this estimate.

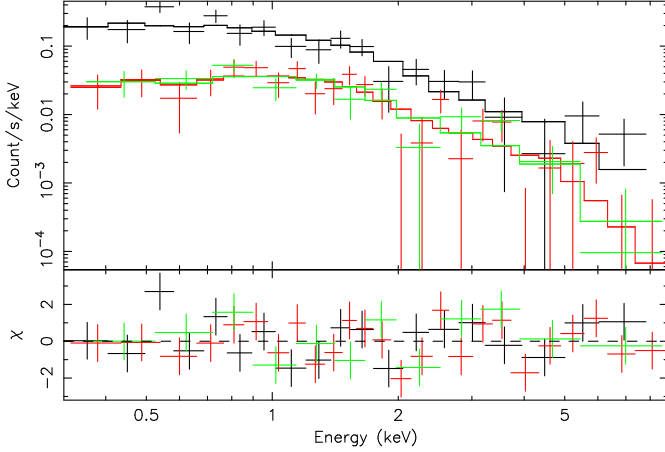


Fig. 15. Spectral fit and residuals for RXJ1701.3; black - PN, dark & light grey - MOS

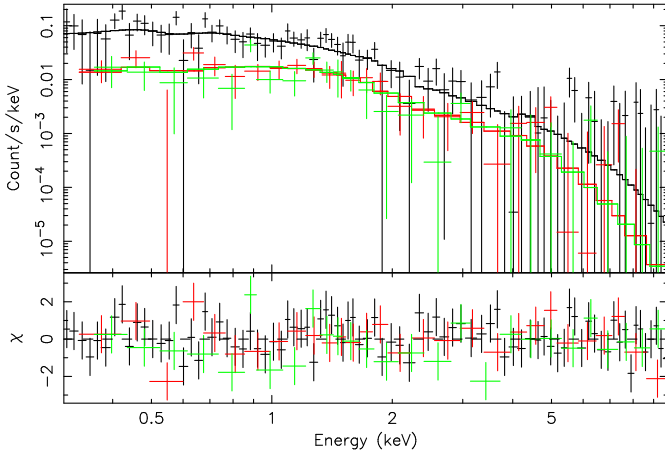


Fig. 16. Spectral fit and residuals for RXJ1354.2 black - PN, dark & light grey - MOS

4.8. RXJ1354.2–0222

The RXJ1354.2–0222 field is shown in Figure 7(d). A point source that was removed during analysis is circled and its position listed in Table A.1. Figure 20 shows the corresponding radial surface brightness distribution and best fit β model that gives $\beta = 0.68 \pm 0.06$ and $r_c = 33.6^{+4.9}_{-3.6}$ arcseconds. ($r_c = 248^{+36}_{-26} h_{50}^{-1}$ kpc, Table 5).

From a spectral extraction region with a radius of $120''$, and using the in-field background subtraction technique, we measured; $T_x = 3.66^{+0.6}_{-0.5}$ keV, $Z = 0.25 \pm 0.14$, (Figure 16). The overall χ^2_ν of the spectral fit was 120 / 147 degrees of freedom. The fixed Galactic hydrogen column value was $N_H = 3.4 \times 10^{20}$ atoms cm^{-2} , but $N_H = 3.2 \pm 1.2 \times 10^{20}$ atoms cm^{-2} when free. The redshift best fit value was 0.53 ± 0.04 . Similarly to RXJ1701.3, we were unable to apply the double-background subtraction technique to these data because of the enhanced proton background (see Figure 5).

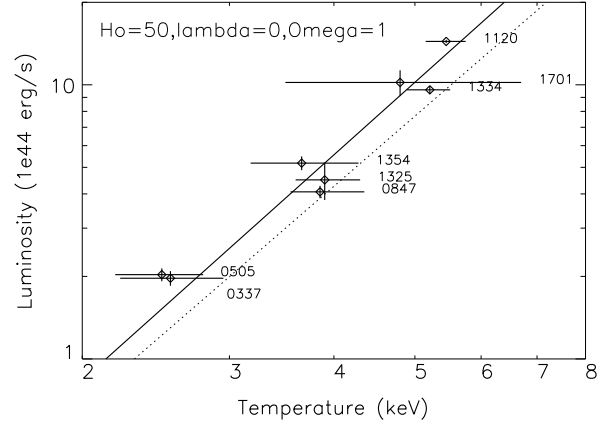


Fig. 17. $L_x - T_x$ relation for an EdS model ($q_0 = 0.5$) and $H_0 = 50 \text{ km s}^{-1} \text{ Mpc}^{-1}$. The solid line is the best fit for our sample after cooling flow excision, the dotted line is the relation from Markevitch (1998) for low red-shift clusters.

5. Discussion

5.1. Luminosity-Temperature Relations

Table 5 summarizes our analysis of the eight cluster observations described above. The mean elemental abundance ($Z = 0.28 \pm 0.08$), core radius ($r_c = 195 \pm 50 h_{50}^{-1}$ kpc) and β ($\beta = 0.70 \pm 0.05$), are consistent with typical values measured at low redshift (e.g. Fukazawa et al., 1998; Jones & Forman, 1999; Mohr, Mathiesen, & Evrard, 1999). The clusters were derived from well understood surveys (SHARC and 160SD) and thus should be representative of the cluster population as a whole at these redshifts. We have used our observations to determine the $L_x - T_x$ relation at $0.45 < z < 0.62$ and to investigate evolutionary effects. We plot luminosity versus temperature, with one sigma errors, for the 8 cluster targets in Figure 17, using the values T_x^{cf} , L_x^{cf} of Table 5. The errors are clearly dominated by those of the temperature measurements.

Characterizing the $L_x - T_x$ relation as

$$L_x = L_6 \left(\frac{T}{6 \text{ keV}} \right)^\alpha \quad (1)$$

and assuming an EdS cosmology, we find $\alpha = 2.7 \pm 0.4$, and $L_6 = 15.9^{+7.9}_{-5.5} \times 10^{44} \text{ erg s}^{-1}$ using the bisector variant of the BCES fitting package (Akritas & Bershady, 1996). This relation is shown as the solid line on Figure 17. The slope of the relation is similar to most previous measurements, e.g. for an EdS cosmology, $\alpha = 2.64 \pm 0.27$ (Markevitch, 1998); $\alpha = 2.33 \pm 0.43$ (Allen & Fabian, 1998); $\alpha = 2.88 \pm 0.15$ (Arnaud & Evrard, (1999)); $\alpha = 2.47 \pm 0.14$ (Ikebe et al., 2002); $\alpha = 2.82 \pm 0.32$ (Novicki, Sornig, & Henry, 2002).

To characterize the possible evolution with z , we assume

$$L_x = L_6 \left(\frac{T}{6 \text{ keV}} \right)^\alpha (1+z)^A \quad (2)$$

Adopting the low redshift $L_x - T_x$ relation from Markevitch (1998) ($\alpha = 2.64 \pm 0.27$, $L_6 = 12.44 \pm 1.08 \times 10^{44} \text{ erg s}^{-1}$) we performed a χ^2 minimization on our data points corrected by a $(1+z)^A$ term. The Markevitch (1998) relation was derived from ROSAT and ASCA observations of 30 clusters at $0.04 < z < 0.1$ ($\bar{z} = 0.05$) and is plotted as a dotted line in Figure 17. On average, the XMM-Newton data points lie away from the Markevitch (1998) relation, suggesting an evolutionary effect whereby clusters of the same temperature were more luminous in the past. The best fit value for A is 0.68 ± 0.26 ($\chi_{\text{red}}=1.2$). We have also determined the BCES best fit for our sample when all the points are corrected with this evolution to a single redshift (low redshift $z = 0.05$ of Markevitch) bin, and find $\alpha = 2.71 \pm 0.22$, and $L_6 = 12.5^{+4.9}_{-3.5} \times 10^{44} \text{ erg s}^{-1}$. We note that we have chosen to compare with Markevitch (1998), rather than with the recent study of 82 clusters with ASCA temperatures by Ikebe et al. (2002), because the Markevitch (1998) method to derive cluster temperatures is closer to our own (Section 5.2.3), thus we try to minimise any systematic effects from different data treatment. In Figure 18 we re-plot our data and the Markevitch (1998) relation after converting them to a common cosmology of $H_0 = 70 \text{ km s}^{-1} \text{ Mpc}^{-1}$, $\Omega_\Lambda = 0.7$, $\Omega_M = 0.3$. In this cosmology we find $A = 1.52^{+0.26}_{-0.27}$.

For comparison, we include the data points obtained by Vikhlinin et al. (2002) from a compilation of Chandra observations of high- z clusters ($0.39 < z < 1.26$) on Figure 18 (after adjusting to $H_0 = 70 \text{ km s}^{-1} \text{ Mpc}^{-1}$). From this Figure, it is clear that both the XMM-Newton and Chandra points lie away from the Markevitch (1998) relation and that there is no obvious systematic offset between the XMM and Chandra data (see Section 5.2.3). Vikhlinin et al. (2002) also used Markevitch (1998) as a low redshift benchmark to investigate $L_x - T_x$ evolution. From their data, Vikhlinin et al. (2002) found $A = 0.6 \pm 0.3$ for $\Omega_\Lambda=0$, $\Omega_M=1$ and $A = 1.5 \pm 0.3$ for a $\Omega_\Lambda = 0.7$, $\Omega_M = 0.3$ cosmology.

The value of A has important implications for our understanding of structure formation and cluster evolution. In a self-similar model (Kaiser, 1981) cluster X-ray properties are driven by gravitational processes, such as shock heating, and a value of $A \sim 1.5$ would be expected in most cosmological models. A self-similar EdS model predicts exactly 1.5, and the value is only slightly different in a low density concordance model, the correction due to the redshift dependence of the virial density (Bryan and Norman, 1998) being small. In a model where the cluster X-ray properties are influenced by non-gravitational processes, such as energy injection by AGN's or supernovae, lower values of A are predicted (e.g. Tozzi & Norman, 2001). The evolution deduced from our observations assuming an EdS model is significantly below the predicted value. Adopting a low density concordance model, on the other hand, leads to a value consistent with predictions. We conclude that there is now evidence from both XMM-Newton and Chandra for an evolutionary trend in the $L_x - T_x$ relation.

Previous studies of $L_x - T_x$ evolution based on either ASCA (e.g. Mushotzky & Scharf, 1997; Allen & Fabian, 1998; Novicki, Sornig, & Henry, 2002; Sadat et al., 1998), ROSAT PSPC (e.g. Fairley et al., 2000) or Chandra (e.g. Borgani et al., 2001; Holden et al., 2002) temperature

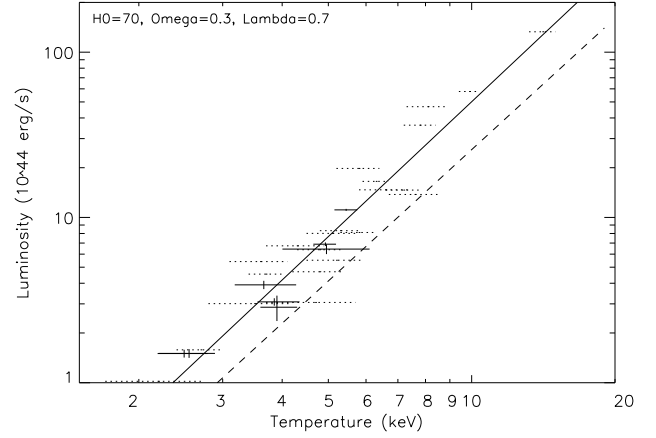


Fig. 18. $L_x - T_x$ relation for $H_0=70$ $\Omega_\Lambda = 0.7$, $\Omega_M=0.3$. The dotted horizontal lines are the CHANDRA sample reported by Vikhlinin et al., 2002, and the dashed diagonal line the Markevitch (1998) $L_x - T_x$ relation corrected to this cosmology. The solid crosses indicate the results from the clusters in our study, corrected for this cosmological model, and the diagonal solid line is the best fit for our data.

measurements found results consistent with no evolution (Sadat et al., 1998). When these studies quote values for A , these values are generally smaller than those measured by us or Vikhlinin et al. (2002), but are usually still at least one sigma away from $A = 0$. Sadat et al. (1998) found a positive evolution $A = 0.5 \pm 0.3$ for $\Omega_M = 1$, $\Omega_\Lambda = 0$ and Novicki, Sornig, & Henry (2002) $A = 1.1 \pm 1.1$ for $\Omega_M = 1$, $\Omega_\Lambda = 0$, and $A = 2.1 \pm 1.0$ for $\Omega_\Lambda=0.7$, $\Omega_M=0.3$ respectively. It is clear that we are beginning to probe evidence that $L_x - T_x$ evolution, although many more clusters need to be studied, and systematic biases (see below) examined in detail, before solid conclusions regarding structure formation models can be drawn.

5.2. Data Treatment and Systematics

We have made every effort to ensure that the $L_x - T_x$ relation presented above is robust. We have adopted a uniform approach to the spatial and spectral analysis of the eight clusters in the sample. We have excised regions with clear signs of point source contamination before extracting spectra and surface brightness profiles. We have not used β -models to calculate total cluster count rates, but have rather summed up the counts within a viral radius. We have tried to ensure that our approach to background subtraction does not bias the measured cluster parameters (see below). We have used measured temperatures to make conversions between count rates and fluxes and, where possible, we have used data from all three EPIC cameras to derive L_x and T_x values. For RXJ0847.2 and RXJ1325.5, data were not available from all three cameras. However, we are confident that the derived quantities for these two clusters are robust, as we have shown, using the RXJ1120.1

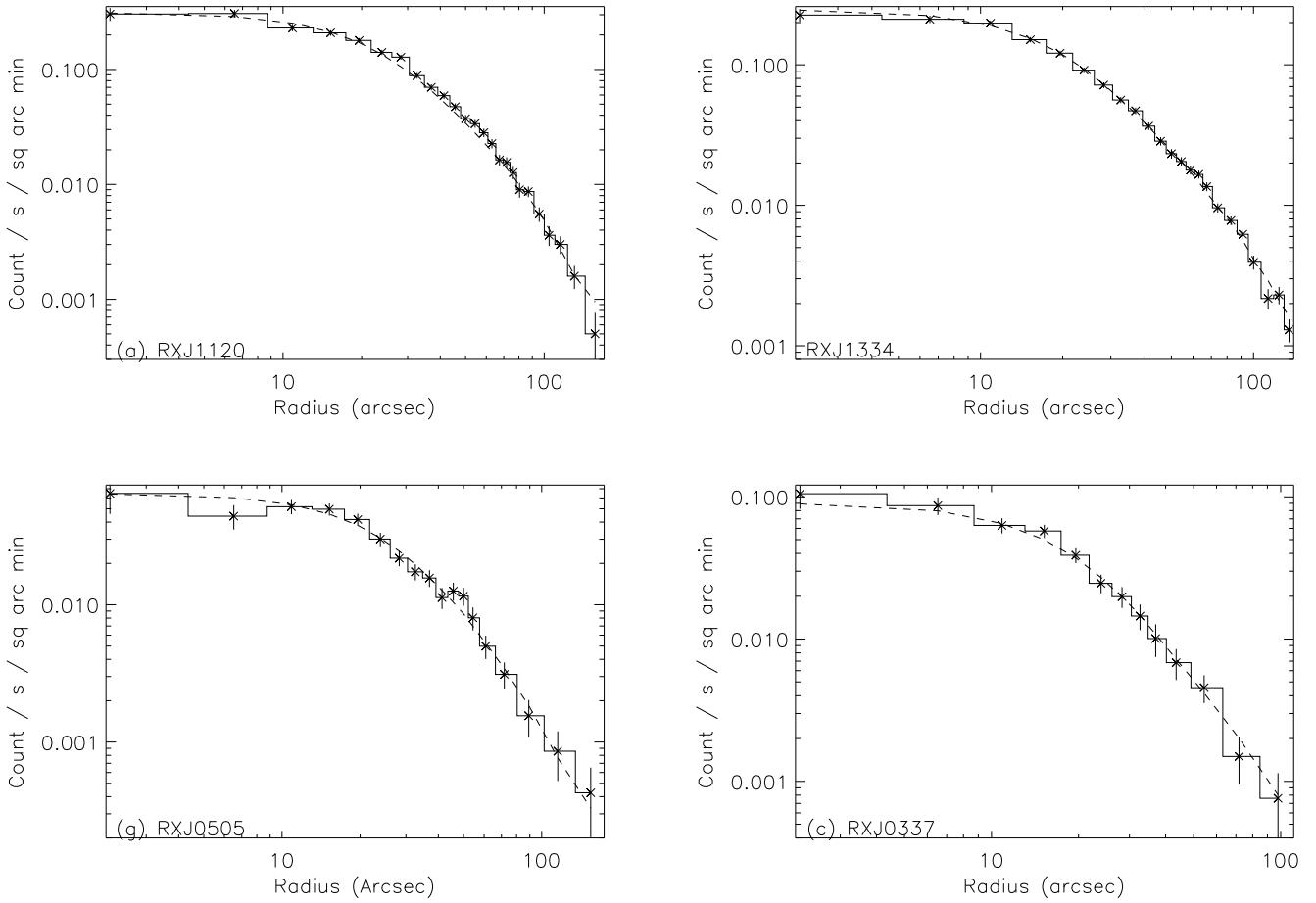


Fig. 19. Surface brightness distribution of clusters, compared with best β -model fit (dotted line). Reading clockwise from top left: RXJ1120.1, RXJ1334.3, RXJ0337.7 and RXJ0505.3.

observation, that PN-only or MOS-only spectra are in excellent agreement.

The background subtraction has been complicated by the extended nature of the targets and the high proton flare contamination in some of the observations. We used background template files during the spatial analysis. These files covered a limited energy range (0.3–4.5 keV), to minimize any calibration uncertainties. They were filtered using the same rate filtering criteria as their respective cluster observation and were normalized to it using the particle background rates in the CCD regions outside the FOV. For various reasons (see Section 3.3), we did not use the background templates for the spectral analysis. Instead, we adopted an in-field background subtraction technique. With this method comes the concern that the proton background can be over-vignetted. We have checked for this by applying a different method, the double subtraction technique, to the RXJ1120.1 and RXJ1334.3 observations. We found that the results from both techniques agree within the statistical errors. For the two observations with the worst proton flare contamination, RXJ1354.2 and RXJ1701.3, we applied a 2% scaling to the in-field background spectrum to compensate for potential over-vignetting of the proton background. In Figure 5

we demonstrate that this over-vignetting should not present a problem for the other clusters in our sample.

Despite all these quality controls, we still cannot rule out the possibility of there being some systematic bias in our results. We discuss possible sources of such bias and the potential impact on our claimed $L_x - T_x$ evolution below.

5.2.1. Impact of Cooling Core Clusters

Cooling cores have the joint effect of boosting the cluster luminosity and of reducing the measured global cluster temperature. These effects have been shown to introduce scatter in the $L_x - T_x$ relation and to modify its slope (Markevitch, 1998; Allen & Fabian, 1998). Various approaches have been taken to alleviate the effects of cooling cores on measured $L_x - T_x$ relations, e.g. by excluding cooling core clusters from the analysis (Arnaud & Evrard, 1999), by fitting two temperature models (Ikebe et al., 2002), by masking the central regions from obvious cooling core clusters (Vikhlinin et al., 2002), or by masking the central regions from all clusters (Markevitch, 1998). Based on the images (Figures 6 & 7) and radial profiles (Figures 19 & 20) of the eight clusters in our sample, we do not

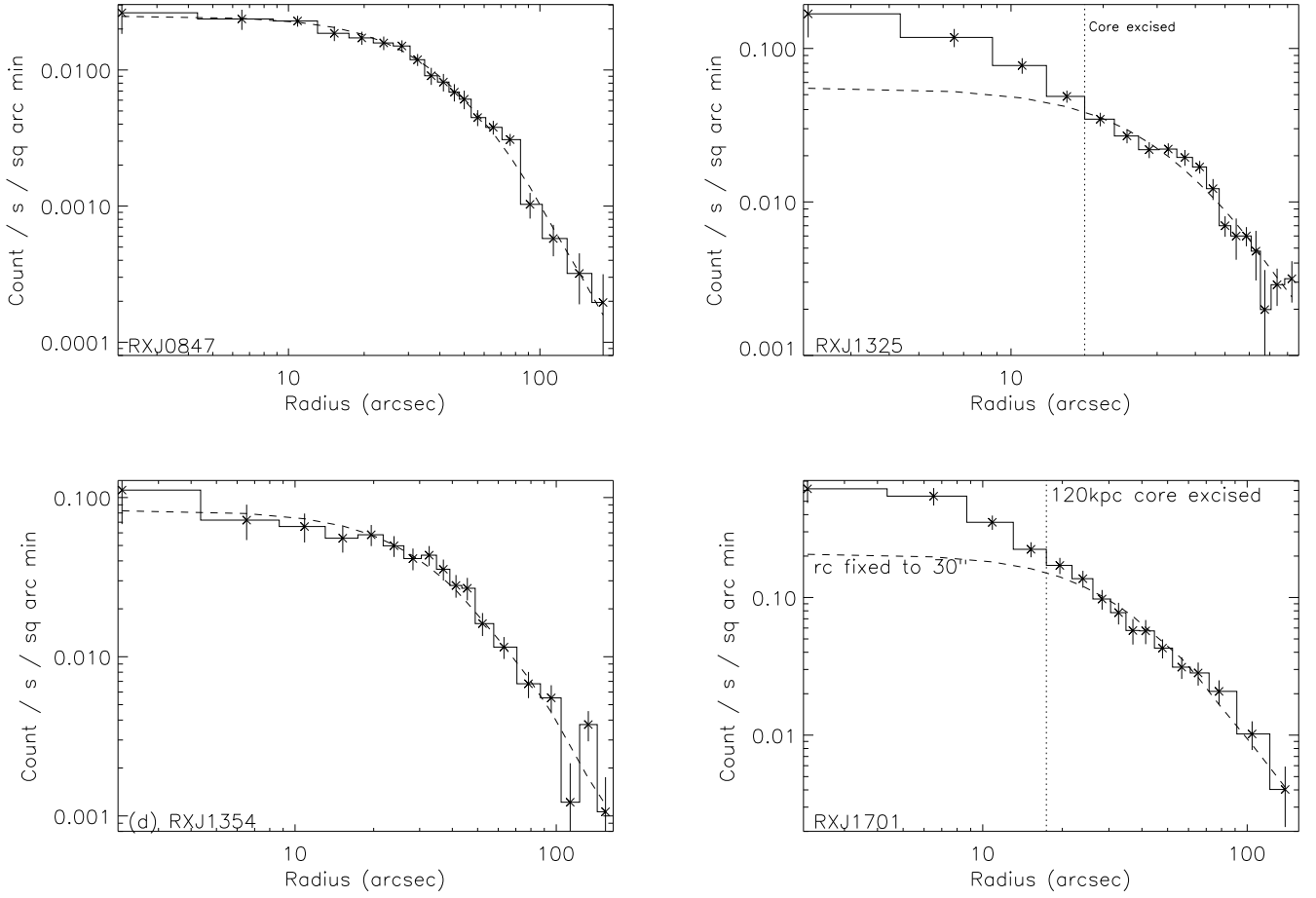


Fig. 20. Surface brightness distribution of clusters, compared with best β -model fit (dotted line). Reading clockwise from top left: , RXJ0847.2, RXJ1325.5, RXJ1701.1 and RXJ1354.2.

expect cooling cores to have much, if any, impact on the measured L_x and T_x values; only RXJ1701.3 and RXJ1325.5 show evidence of a central surface brightness excess. We have investigated this by comparing the results before and after excising a circular region⁴ from the cluster cores.

The results of the re-analysis can be found in Table 5, (rows 4 and 5). Temperatures changed very little – always within the statistical error – after we excised the central $r = 50h_{50}^{-1}$ kpc region. In two cases, (RXJ1120.1 and RXJ1701.3), the luminosity changes by more than 1σ , but still by only 5% and 9% respectively. Without the excision the best fit $L_x - T_x$ relation is $L_6 = 17.6^{+5.3}_{-4.1} \times 10^{44} \text{ erg s}^{-1}$ and $\alpha = 2.66 \pm 0.25$ for an $\Omega_\Lambda = 0.0, \Omega_M = 1.0, H_0 = 50 \text{ km s}^{-1} \text{ Mpc}^{-1}$ cosmology at a typical redshift $z \sim 0.55$. In summary, we find the $L_x - T_x$ relations before and after the core excision are consistent within the errors. However, we caution that some residual cooling flow contamination may still remain after this excision; $50h_{50}^{-1} \text{ kpc} \approx 14''$, corresponding to an encircled energy fraction of a little under 50% of the on-axis mirror PSFs.

⁴ The radius of the excised region was $50 h_{50}^{-1}$ kpc except in the case of RXJ1701.3 and RXJ1325 where $\sim 120 \text{ kpc}$ was used, see sections 3.6 and 3.7

5.2.2. Incompleteness and Flux Errors in the ROSAT Catalogs

Our $L_x - T_x$ evolution result implies that high redshift clusters in our sample are more luminous than clusters of the same temperature at lower redshift. We interpret this as evidence for a general evolutionary trend in the $L_x - T_x$ relation, but it might also reflect an underlying selection bias in the cluster catalogs from which the sample was drawn, e.g. if the SHARC and 160SD surveys were biased toward merging systems. It is possible that the luminosity and temperature of clusters can change dramatically during the process of a major merging event (Ricker & Sarazin, 2001). Based on the XMM-Newton images of the 8 clusters studied here (Figures 6 & 7), such a bias does not appear to exist; only RXJ1354 has evidence for a possible double component, and excluding this from the best fit $L_x - T_x$ relation changes the luminosity normalisation only $\sim 2\%$. As long as the angular resolution of observations allows sufficient discrimination against obvious mergers, then presumably an ensemble sample of local and distant clusters are similarly affected by merger boosting of luminosity.

Moreover, we find no evidence for any incompleteness in the SHARC and 160SD surveys, at least in the small area covered by these observations. No new clusters were found in the fields surrounding the seven SHARC clusters in our sample. In the field of the 160SD cluster, RXJ0847.2, we have discovered a new X-ray cluster (XMMU J084701.8+345117). However this cluster was too faint to have been included in the original 160SD survey. We estimate the ($r < r_v$) flux of this object to be $1.3 \times 10^{-14} \text{ erg cm}^{-2} \text{ s}^{-1}$ (based on a fitted temperature of $T_x = 1.8 \text{ keV}$ and an assumed redshift of $z = 0.56$), compared to the 160SD flux limit of $3.7 \times 10^{-14} \text{ erg cm}^{-2} \text{ s}^{-1}$, so this cluster is too faint to have been included in the original 160SD survey. In summary we do not find evidence for any intrinsic bias in the SHARC or 160SD survey selection functions that could mimic $L_x - T_x$ evolution.

Another possible way to mimic the claimed evolution would be to systematically overestimate the L_x values. We have investigated this by comparing our flux measurements to those published in several works (Romer et al., 2000; Burke et al., 2003; Vikhlinin et al., 1998). We report here that a systematic offset does appear to exist, but in the opposite direction to that needed to mimic evolution. The XMM-Newton fluxes quoted in Table 5 are all lower than previously determined values, typically by 20% but as much as by 40% in the case of RXJ0505.3. We note that this discrepancy persists regardless of the ROSAT catalog from which the cluster was selected. The average discrepancy between the Southern SHARC (4 clusters), Bright SHARC (3 clusters) and 160SD (3 clusters) fluxes and the XMM-Newton fluxes is 22%, 21% and 16% respectively.

Improvements in point source rejection, count rate to flux conversions and the signal to noise have meant that the typical statistical error on the XMM-Newton determined fluxes in Table 5 is $\approx 3\%$, compared to $\approx 10\%$ for the ROSAT determinations. Therefore, even accounting for a possible offset in the absolute cross calibration of the two observatories, it is clear that a systematic flux offset does exist. There are likely to be several reasons for this offset. Of these, the use of an incorrect spatial model, to convert between an aperture flux and a total flux, is probably the most significant. As shown in Romer et al., 2000, the use of a generic ($\beta = 0.67$, $r_c = 250h_{50}^{-1} \text{ kpc}$), rather than best fit, β -model resulted in a typical enhancement of 10% in the total cluster flux. In our XMM-Newton analysis, we do not use the β -model fits to determine the total flux. Instead we directly sum up the counts within a virial radius. For some clusters this difference in approach can explain the entire ROSAT to XMM-Newton discrepancy. For example, in the case of RXJ1334.3, our estimate of r_v is almost identical to the r_{80} radius within which 80% of the total flux from a generic β -model would fall. Romer et al., 2000 divided the ROSAT counts within r_{80} by 0.8 to estimate the total count rate. For RXJ1334.3 this division would artificially boost the flux by 25% which more than accounts for the 22% the discrepancy between the XMM-Newton and Bright SHARC values.

For the four Southern SHARC clusters in our sample, we have recalculated the total ROSAT PSPC fluxes using the β and r_c values given in Table 5 (in Burke et al., 2003 generic values were used; $\beta = 0.67$, $r_c = 250h_{50}^{-1} \text{ kpc}$). By doing so,

we improve the consistency between the ROSAT and XMM-Newton fluxes to within 5% for RXJ1354.2 and RXJ1325.5 and within 15% for RXJ0337.7. For RXJ0505.3 there remains a large, 35%, discrepancy which requires further investigation.

For the three Bright SHARC clusters in our sample, we have gone back to the original Romer et al., 2000 data and measured count rates inside r_v . Doing so reduces the ROSAT determined flux by $\approx 30\%$ in the case of both RXJ1120.1 and RXJ1334.3, i.e. so that they are $\approx 10\%$ lower than the values quoted in Table 5. In the case of RXJ1701.3, the measured ROSAT flux actually increased slightly when measured inside r_v rather than r_{80} . On closer examination of the ROSAT data, it was apparent that the nearby QSO and cluster (see Figure 7) were contaminating both the source and background apertures in the PSPC image. When the source and background were accumulated only from the (source free) region to the West of the cluster, the ROSAT flux within r_v dropped to within $\approx 10\%$ of the XMM-Newton determined value. These examples demonstrate the importance of using XMM-Newton to re-calculate fluxes and luminosities for high redshift clusters detected at low signal to noise by ROSAT. We stress that, despite these flux uncertainties, the SHARC and 160SD catalogs are still fair representations of the underlying cluster population and can still be used to probe the $L_x - T_x$ relation. It is also important to note that these flux uncertainties do not apply to the ROSAT observations used by Markevitch, 1998 to determine L_x values for the 30 low redshift clusters in his $L_x - T_x$ analysis. Those observations have exquisite signal to noise, so that the L_x values derived from them will be limited only by the absolute calibration of the instrument.

The fact that we find a $L_x - T_x$ relation consistent with the low redshift value argues against a bias in our selection towards the more luminous tail of the cluster population; for either

- all the clusters must be biased in the same way, or
- they are biased in just such a way as to offset any real evolution in the value of the slope.

Nevertheless the reader might be cautioned that should there remain a common bias for all cluster samples, despite these cross-checks, it is possible the clusters selected represent the brightest portion of the intrinsic high-z sample, and thus remain on the high luminosity end of the true population, hence mimicking the luminosity evolution we see. Further validation of the ROSAT data with CHANDRA and XMM-Newton should help to close this issue.

5.2.3. Comparison with Markevitch (1998) and Vikhlinin et al. (2002)

We come to very much the same conclusions regarding $L_x - T_x$ evolution as did Vikhlinin et al., 2002. Given that these conclusions provide evidence for significant evolution, contrary to previous analyses, it is important to investigate whether this concordance is genuine or coincidental. Both studies rely on Markevitch, 1998 for the low redshift comparison, so let us first consider how our XMM-Newton clusters might appear either too luminous, or too cool, compared to the Markevitch, 1998 sample:

1. Markevitch 1998 measured cluster fluxes by summing the count rate inside circular apertures. However, rather than using a cluster specific virial radius, he used a fixed metric aperture of $r = 1h_{50}^{-1}$ Mpc and ignored any flux that might lie outside this radius. However, this would be a very small effect; Vikhlinin et al. (2002) estimate that the no more than 4% of the total flux would be missed by adopting a fixed $r = 1h_{50}^{-1}$ Mpc aperture.
2. When Markevitch 1998 excised the central $r = 50h_{50}^{-1}$ kpc region from all the clusters in his low redshift sample before measuring the flux, he applied a multiplication factor of 1.06 to account for flux falling inside the excised region. We carried out an excision and flux lost correction on our eight clusters with a cluster-specific surface brightness model. (Section 5.2.1, and Table 5), we found that for six of the eight clusters, the measured L_x values dropped slightly. The difference in our techniques could systematically affect cluster brightness, compared with the low redshift counterparts, but only at the few percent level.
3. Uncertainties in the cross calibration between XMM-Newton and the instruments used for the Markevitch, 1998 analysis (ROSAT and ASCA) may mimic evolution in the $L_x - T_x$ relation. At this time it is not possible to rule out that possibility; to date, a full comparison of XMM-Newton and ASCA determined cluster temperatures has not been carried out.
4. Ikebe et al., 2002 have used a different approach to Markevitch, 1998 to analyse ASCA observations of low redshift clusters. They measure temperatures that are on average lower than those measured by Markevitch, 1998, with the trend becoming more pronounced as T_x increases. However, this should not impact our conclusions regarding $L_x - T_x$ evolution, given that we used a similar technique to Markevitch, 1998 to measure T_x .
5. Some estimate of the effect of external systematic error *could* be taken by considering the value of A in fitting to a different low- z $L_x - T_x$ sample. We have done so using the Arnaud & Evrard, (1999) relation and find $A = 0.95 \pm 0.2$ (again in the Einstein de Sitter cosmology). Therefore, despite a possible contamination in that sample from cooling flows we still see evidence for evolution

We note that the first two concerns listed above do not apply to the Vikhlinin et al., (2002) study, as they deliberately adopted the same methodology as Markevitch, 1998 and the last three concerns are not likely to be important either; Vikhlinin et al., (2002) have carried out a cross comparison of Chandra and ASCA T_x values for ≈ 20 low redshift clusters and find them to be in agreement at better than the 5% level, with no systematic offset. Despite this, we should still consider the possibility that both studies (ours and Vikhlinin et al., 2002) might be pointing to the wrong value of A . At present we cannot quantify how factors such as uncertainties in the cross-calibration of Chandra and XMM-Newton, especially at low energies, might impact our conclusions. We note in particular that Vikhlinin et al., (2002) applied an empirical factor of 0.93 to improve the cross-calibration of the ACIS front- and back-illuminated CCDs below 1.8keV. Other differences between the observa-

tories may also be important. For example, it will be easier to account for point source and cooling core contamination using Chandra data, because of the improved spatial resolution (see for example the case of RXJ1701.3). Alternatively, it should be easier to correctly account for the various particle (cosmic ray and proton) backgrounds using XMM-Newton data, because its CCD's cover a larger area both inside and outside the FOV. In summary, although we cannot rule out the possibility that a combination of factors have lead us to measure an artificially large value for the A parameter, we believe that our XMM measurements provide clear evidence for evolution in the $L_x - T_x$ relation.

6. Acknowledgments

We thank M Arnaud for very useful comments concerning the analysis and interpretation of the data. We also thank M Markevitch and A. Vikhlinin for their assistance. M Watson is acknowledged for allowing us to use data from the GT observation of IRAS 13224-3809. The EPIC instrument team are thanked for their continued help in improving the calibration knowledge and help in understanding various effects related to the instrument background. We thank the referee, F Castander for the careful review and comments that helped to improve the interpretations. DJB acknowledges the support of NASA contract NAS8-39073 (CXC). AKR and RCN acknowledge support from the NASA-LTSA program, contract NAG5-11634 and the hospitality of the Durham University Physics department during the summer of 2002. These data were obtained from observations made by the *XMM-Newton* Observatory. This is an ESA science mission with instruments and contributions directly funded by ESA Member States and the USA (NASA). The XMM-Newton Ω Project GT data were provided from a combination of data-rights holders, including the CDS Strasbourg (XMM Science Survey Centre), CEA-Saclay (XMM EPIC PI Team) and the XMM-Newton SOC.

References

- Adami, C., Ulmer, M.P., Romer, A.K. et al., 2000, *ApJS*, 131, 391
- Akritas, M.G., & Bershad, M. A., 1996, *ApJ*, 470, 706
- Allen, S. W. & Fabian, A. C. 1998, *MNRAS*, 297, L57
- Arnaud, K. in *Astronomical Data Analysis Software and Systems V*, 1996, A.S.P. Conf. Ser., 101, G. Jacoby & J. Barnes, eds., 17
- Arnaud, M. & Evrard, E. 1999, *MNRAS*, 305, 631
- Arnaud, M., Neumann, D. M., Aghanim, N., et al., 2001, *A&A*, 365, L80
- Arnaud, M., Majerowicz, S., Lumb, D.H. et al., 2002, *A&A*, 390, 27
- Bartlett, J. G., Aghanim, N., Arnaud, M. et al. 2001, *Proc. 21st Moriond Astrophys. meeting*, ed. D. M. Neumann & J. Tranh Thanh Van
- Blanchard, A. & Bartlett, J.G., 1998, *A&A*, 314, 13
- Blanchard, A., Sadat, R., Bartlett, J.G. & Le Dour, M., 2000, *A&A*, 362, 809
- Borgani, S., Rosati, P., Tozzi, P. & Norman, C., 1999, *ApJ*, 517, 40
- Borgani, S., Rosati, P., Tozzi, P. et al., 2001, *ApJ*, 561, 13
- Bryan, G.L. & Norman, M.L., 1998, *ApJ*, 495, 80
- Burke, D.J., Collins, C.A., Sharples, R.M. et al., 1997, *ApJ*, 488, L83
- Burke, D. J., Collins, C. A., Sharples, R. M., Romer, A. K., & Nichol, R. C., 2003, *MNRAS*, 341, 1093

	RXJ0337.7	RXJ0505.3	RXJ0847.2	RXJ1120.1	RXJ1325.5	RXJ1334.3	RXJ1354.2	RXJ1701.3
centroid RA	03:37:45	05:05:19	08:47:10	11:20:07	13:25:37	13:34:20	13:54:17	17:01:24
centroid Dec	-25:22:32	-28:48:50	+34:48:54	+43:18:04	-38:25:44	+50:31:02	-02:21:44	+64:14:12
Cooling Flow Excised								
T_x^{cf} (keV)	2.52 +0.36 -0.32	2.56 ±0.3	3.91 +0.5 -0.35	5.35 +0.42 -0.32	3.77 +0.4 -0.36	4.98 +0.26 -0.32	3.86 +0.62 -0.55	4.8 +1.9 -1.3
L_{bol}^{cf} 10^{44} erg s $^{-1}$	1.91 ±0.17	1.97 ±0.16	3.89 ±0.7	13.7 ±0.23	4.2 ±0.8	9.47 ±0.24	5.3 ±0.4	10.2 ±1.1
No Cooling Flow Excision								
T_x (keV)	2.6 ± 0.35	2.5 ±0.3	3.62 +0.58 -0.51	5.45 ±0.3	4.15 +0.4 -0.3	5.20 +0.26 -0.28	3.66 +0.6 -0.5	4.5 +1.5 -1.0
L_{bol} 10^{44} erg s $^{-1}$	1.97 ±0.1	2.03 ±0.11	4.07 ±0.2	14.4 ±0.2	4.5 ±0.7	9.59 ±0.27	5.18 ±0.3	11.1 ±1.0
Flux (0.5–2) 10^{-14} cgs	4.37 ±0.2	5.64 ±0.2	7.04 ±0.3	24.5 ±0.54	8.0 ±0.03	14.1 ±0.2	9.8 ±0.5	24 +1.5 -1.2
N_H (10^{20}) (atom cm $^{-2}$)	0.99	1.5	3.2	2.1	4.8	1.05	3.4	2.6
β	0.76 +0.08 -0.04	0.66 +0.05 -0.04	0.81 ±0.045	0.77 ±0.03	0.64 +0.09 -0.07	0.66 ±0.02	0.68 ±0.055	0.64 ±0.05
r_c (kpc)	145	164	307	209	115	154	248	204
h_{50}^{-1}	±18	± 17	±30	+9 -8	±20	±10	+36 -26	fixed
Abundance (Z)	0.38 ±0.09	0.17 ±0.08	0.30 ±0.28	0.47 ±0.09	0.31 +0.19 -0.17	0.15 ±0.08	0.25 ±0.14	0.24 ±0.2
z (optical)	0.577	0.51	0.56	0.60	0.445	0.62	0.551	0.45
Normaln. mekal 10^{-4}	1.68 ±0.10	2.12 ±0.08	2.65 +0.12 -0.11	9.42 +0.23 -0.17	2.7 +0.08 -0.07	5.61 ±0.16	4.01 +0.14 -0.23	5.58 +0.50 -0.40
Radius (")	120	120	120	145	90	120	120	120
Spect. extract.								
Fract $_r$ counts within r_v	0.90	0.87	0.79	0.965	0.52	0.84	0.83	0.81

Table 5. Summary of cluster parameters for EdS model $H_0=50$, $q_0=0.5$. Spectral fitting errors, $L_x\beta$ and r_c are 1σ on one parameter. Fluxes are the measured, absorbed fluxes in ROSAT band. Fract $_r$ is the fractional correction made from the spectral extraction region, to the total counts within the r_v radius after accounting for point source excision, inter-chip gaps loss etc.. The 3rd & 4th rows summarise the data for the case when the core region has been excised from the cluster core. (Except for RXJ1701.3, where following the CHANDRA data, we excise a cooling flow enhancement to 120kpc).

- Collins, C.A., Burke, D.J., Romer, A.K. et al. 1997., ApJ, 479, L117
Dickey, J.M. & Lockman, F.J., 1990, ARA&A, 28, 215
Ebeling, H., Edge, A. C., & Henry, J. P., 2001, ApJ, 553, 668
Edge, A.C., Stewart, G.C., Fabian A.C. & Arnaud, K.A., 1990, MNRAS, 245, 559
Eke, V.R., Cole, S., Frenk C.S. & Henry, J.P., 1998, MNRAS, 298, 1145
Evrard, A.E., Metzler, C.A. & Navarro, J.F., 1996, ApJ, 469, 494
Fairley, B., Jones, L., Scharf, C. et al., 2000, MNRAS, 315, 669
Fukazawa, Y., Makishima, K., Tamura, T. et al., 1998, PASJ, 50, 187
Gioia, I.M., Maccacaro, T., & Schild, R.E., 1990, ApJS, 72, 567
Gioia, I. M., Henry, J. P., Mullis, C. R., Voges, W., Briel, U. G., Böhringer, H., & Huchra, J. P., 2001, ApJ, 553, L105
Ikebe, Y., Reiprich, T. H., Böhringer, H. et al., 2002, A&A, 383, 773
Jones, C. & Forman, W., 1999, ApJ, 511, 65
Henry, J.P., 1997, ApJ, 489, L1
Henry, J.P., 2000 ApJ., 534, 565
Henry, J.P. & Arnaud, K.A., 1991, ApJ, 372, 410
Henry, J. P., Gioia, I. M., Mullis, C. R., Voges, W., Briel, U. G., Böhringer, H., & Huchra, J. P. 2001, ApJ, 553, L109
Holden, B. P., Stanford, S. A., Squires, G. K., Rosati, P., Tozzi, P., Eisenhardt, P., & Spinrad, H., 2002, AJ, 124, 33
Jansen, F., Lumb, D.H., Altieri, B. et al., 2001, A&A 365, L1
Ikebe, Y., Reiprich, T. H., Böhringer, H., Tanaka, Y., & Kitayama, T., 2002, A&A, 383, 773
Jenkins, A., Frenk, C.S., White S.D.M. et al., 2001, MNRAS, 321, 372
Jones, C. & Forman, W., 1999, ApJ, 511, 65
Lumb, D.H., Warwick, R.S., Page, M., De Luca, A., 2002, A&A 389, 93
Kaiser, N., 1991, ApJ, 383, 104
McCammon, D. & Sanders, D.T., 1990, ARA&A, 28, 657
Maddox, S.J., Sutherland, W.J., Efstathiou, G. & Loveday, J. 1990, MNRAS, 243, 692
Majerowicz, S., Arnaud, M., Lumb, D. & Neumann, D. 2002, in Proc. of the Symposium “New Visions of the X-ray Universe in the XMM-Newton and Chandra era” ArXiv Astrophysics e-prints, astro-ph/0202220
Majerowicz, S., Arnaud, M., & Neumann, D. M. 2002, Proceedings of the Conference on Matter and Energy in Clusters of Galaxies, Chung-Li (2002), editors: S.Bowyer and C.-Y. Hwang ArXiv Astrophysics e-prints, astro-ph/0207232
Majerowicz, S. et al., 2004, A&A submitted.
Majumdar, S. & Mohr, J.J., 2003, ApJ, 585, 603
Markevitch, M., 1998, ApJ., 504, 27
Markevitch, M. 2002, ArXiv Astrophysics e-prints, astro-ph/0205333
Mewe, R., Lemen, J.R. & v d Oord, G.H.J., 1986, A & AS, 62, 197
Mohr, J. J., Mathiesen, B., & Evrard, A. E., 1999, ApJ, 517, 627
Mullis, C. R., McNamara, B. R., Quintana, H. et al., 2003, ApJ, 594, 154

- Mushotzky, R. F. & Scharf, C. A., 1997, *ApJ*, 482, L13
- Nevalainen, J., Markevitch, M. & Forman, W., 2000, *ApJ*, 532, 694
- Nichol, R.C., Romer, A.K., Holden, B.P. et al., 1999, *ApJ*, 521, L21
- Novicki, M. C., Sornig, M., & Henry, J. P., 2002, *AJ*, 124, 2413
- Oukbir, J. & Blanchard, A., 1992, *A&A*, 262, 21
- Oukbir, J. & Blanchard, A., 1997, *A&A*, 317, 1
- Pratt, G., Arnaud, M. & Aghanim, N., 2001, in Proc. of ‘Galaxy Clusters and the High Redshift Universe Observed in X-rays’, XXIIth Moriond Astrophysics Meeting, astro-ph/0105431
- Press, W.H. & Schechter, P., 1974, *ApJ*, 187, 425
- Rasmussen, A., Chervinsky, J. and Golovchenko, J. 1999, Columbia Astrophysics Laboratory Pre-print, RGS-COL-CAL-99009
- Reichart, D.E., Lamb, D.Q., Metzger, M.R. et al., 1999, *ApJ*, 518, 521
- Ricker, P. M. & Sarazin, C. L., 2001, *ApJ*, 561, 621
- Roettiger, K., Loken, C. & Burns, J.O., 1997, *ApJ*, 307, 109
- Romer, A.K., Nichol, R.C., Holden, B.P. et al., 2000, *ApJS*, 126, 209
- Rosati, P., Della Ceca, R., Burg, R., Norman, C., & Giacconi, R., 1995, *ApJ*, 445, L11
- Sadat, R., Blanchard, A. & Oukbir, J., 1998, *A&A*, 329, 21
- Scharf, C. A., Jones, L. R., Ebeling, H., Perlman, E., Malkan, M. & Wegner, G., 1997, *ApJ*, 477, 79
- Scharf, C., Donahue, M., Voit, G. M. et al., 2000, *ApJ*, 528, L73
- Schindler, S. & Müller, E., 1993, *A&A*, 272, 137
- Struble, M.F. & Rood, H.J., 1991, *ApJS*, 125, 35
- Strüder, L., Briel, U., Dennerl, K. et al., 2001, *A&A*, 365, L18
- Tozzi, P. & Norman, C., 2001, *ApJ*, 546, 63
- Turner, M.J.L., Abbey, A.F., Arnaud, M. et al., 2001, *A&A* 365, L27
- Vauclair, S.C., Blanchard, A., Sadat, R. et al., 2003, *A&A*, 412, L37
- Viana, P.T.P. & Liddle, A.R., 1999, *MNRAS*, 303, 535
- Vikhlinin, A., McNamara, B. R., Forman, W. et al., 1998, *ApJ*, 502, 558
- Vikhlinin, A., VanSpeybroeck, L., Markevitch, M. et al., 2002, *ApJ*, 578, L107
- Wang, L. & Steinhardt, P.J., 1998, *ApJ*, 508, 483
- Watson, M.G., Augeres, J-L., Ballet, J. et al., 2001, *A&A* 365, L51
- Zhang, Y., Finoguenov, A., Boehringer, H., Ikebe, Y., Matsushita, K., & Schuecker, P., 2003, *A&A*, 413, 497

Appendix A: Excised Point Sources

XMM-Newton ID	RA 2000	Dec 2000
Field RXJ0337.7 – 2522		
XMMU J033737.8 – 252318	03:37:37.8	– 25:23:18.0
XMMU J033743.7 – 252326	03:37:43.7	– 25:23:26.7
XMMU J033742.9 – 252208	03:37:42.9	– 25:22:8.4
XMMU J033745.9 – 252206	03:37:45.9	– 25:22:6.2
XMMU J033747.2 – 252214	03:37:47.2	– 25:22:14.9
Field RXJ0505.3 – 2849		
XMMU J050512.5 – 285034	05:05:12.5	– 28:50:34.6
XMMU J050517.3 – 285023	05:05:17.3	– 28:50:23.7
XMMU J050522.3 – 285006	05:05:22.3	– 28:50:06.3
XMMU J050510.9 – 284951	05:05:10.9	– 28:49:51.1
Field RXJ0847.2 + 3449		
XMMU J084711.4 + 344717	08:47:11.4	34:47:17.1
XMMU J084714.5 + 344654	08:47:14.5	34:46:54.4
XMMU J084707.5 + 344947	08:47:7.5	34:49:46.7
XMMU J084709.5 + 344917	08:47:9.5	34:49:17.1
Field RXJ1120.1 + 4318		
XMMU J111959.1 + 432030	11:19:59.1	43:20:30.3
XMMU J112001.3 + 431543	11:20:01.3	43:15:43.2
XMMU J112004.2 + 431932	11:20:04.2	43:19:31.6
XMMU J112008.8 + 432030	11:20:08.8	43:20:30.3
XMMU J112009.6 + 432056	11:20:09.6	43:20:56.4
XMMU J112014.4 + 431932	11:20:14.4	43:19:31.6
XMMU J112015.0 + 432009	11:20:15.0	43:20:08.5
Field RXJ1334.3 + 5030		
XMMU J133426.3 + 503247	13:34:26.3	50:32:46.8
XMMU J133410.8 + 503118	13:34:10.8	50:31:17.6
XMMU J133415.6 + 503030	13:34:15.6	50:30:29.7
XMMU J133416.3 + 503115	13:34:16.3	50:31:15.4
XMMU J133430.2 + 503238	13:34:30.2	50:32:38.0
XMMU J133428.9 + 503141	13:34:28.9	50:31:41.5
Field RXJ1354.2 – 0222		
XMMU J135414.8 – 022031	13:54:14.8	– 02:20:31.7

Table A.1. The identifications (XMM-Newton informal ID, nominal RA & Dec) of point sources that were excised from the spectral and imaging analysis